Acta Pharmaceutica Sinica B 2024;14(2):635−652

Chinese Pharmaceutical Association
Institute of Materia Medica, Chinese Academy of Medical Sciences

Acta Pharmaceutica Sinica B

www.elsevier.com/locate/apsb
www.sciencedirect.com

ORIGINAL ARTICLE

miR-429-3p mediates memory decline by targeting MKP-1 to reduce surface GluA1-containing AMPA receptors in a mouse model of Alzheimer's disease

Man Luo[a], Yayan Pang[a], Junjie Li[a], Lilin Yi[a], Bin Wu[a], Qiuyun Tian[a], Yan He[a], Maoju Wang[a], Lei Xia[a], Guiqiong He[b], Weihong Song[a,c,d], Yehong Du[a,*], Zhifang Dong[a,e,*]

[a]*Pediatric Research Institute, Ministry of Education Key Laboratory of Child Development and Disorders, National Clinical Research Center for Child Health and Disorders, China International Science and Technology Cooperation Base of Child Development and Critical Disorders, Chongqing Key Laboratory of Translational Medical Research in Cognitive Development and Learning and Memory Disorders, Children's Hospital of Chongqing Medical University, Chongqing 400014, China*
[b]*Department of Anatomy, Basic Medical College, Chongqing Medical University, Chongqing 400016, China*
[c]*Townsend Family Laboratories, Department of Psychiatry, The University of British Columbia, Vancouver BC V6T 1Z3, Canada*
[d]*Oujiang Laboratory (Zhejiang Lab for Regenerative Medicine, Vision and Brain Health), Institute of Aging, Key Laboratory of Alzheimer's Disease of Zhejiang Province, Zhejiang Clinical Research Center for Mental Disorders, School of Mental Health and the Affiliated Kangning Hospital, Wenzhou Medical University, Wenzhou 325000, China*
[e]*Institute for Brain Science and Disease of Chongqing Medical University, Chongqing 400016, China*

Received 4 July 2023; received in revised form 24 September 2023; accepted 7 October 2023

KEY WORDS

Alzheimer's disease;
MKP-1;
miR-429-3p;
AMPA receptor;

Abstract Alzheimer's disease (AD) is a leading cause of dementia in the elderly. Mitogen-activated protein kinase phosphatase 1 (MKP-1) plays a neuroprotective role in AD. However, the molecular mechanisms underlying the effects of MKP-1 on AD have not been extensively studied. MicroRNAs (miRNAs) regulate gene expression at the post-transcriptional level, thereby repressing mRNA translation. Here, we reported that the microRNA-429-3p (*miR-429-3p*) was significantly increased in the brain of APP23/PS45 AD model mice and $N2A^{APP}$ AD model cells. We further found that *miR-429-3p* could

*Corresponding authors.
E-mail addresses: zfdong@cqmu.edu.cn (Zhifang Dong), dudu0000807@126.com (Yehong Du).
Peer review under the responsibility of Chinese Pharmaceutical Association and Institute of Materia Medica, Chinese Academy of Medical Sciences.

https://doi.org/10.1016/j.apsb.2023.10.015

Learning and memory;
Long-term potentiation

downregulate MKP-1 expression by directly binding to its 3′-untranslated region (3′ UTR). Inhibition of *miR-429-3p* by its antagomir (A-miR-429) restored the expression of MKP-1 to a control level and consequently reduced the amyloidogenic processing of APP and Aβ accumulation. More importantly, intranasal administration of A-miR-429 successfully ameliorated the deficits of hippocampal CA1 long-term potentiation and spatial learning and memory in AD model mice by suppressing extracellular signal-regulated kinase (ERK1/2)-mediated GluA1 hyperphosphorylation at Ser831 site, thereby increasing the surface expression of GluA1-containing α-amino-3-hydroxy-5-methyl-4-isoxazolepropionic acid receptors (AMPARs). Together, these results demonstrate that inhibiting *miR-429-3p* to upregulate MKP-1 effectively improves cognitive and synaptic functions in AD model mice, suggesting that *miR-429*/MKP-1 pathway may be a novel therapeutic target for AD treatment.

1. Introduction

Alzheimer's disease (AD) is a progressive neurodegenerative disease accompanied by cognitive impairment and is considered the leading cause of dementia in the elderly[1,2]. However, the lack of effective treatments for AD greatly burdens society and patients' families[3]. Abnormal cleavage of amyloid-β (Aβ) precursor protein (APP) by β-secretase (BACE1) and γ-secretase generates Aβ[4–6], and the accumulation of Aβ to form senile plaques in the brain is the pathological hallmark of AD. In addition, recent studies have discovered that APP can be cleaved at a novel cleavage site termed η-site to produce CTF-η[7,8]. It is well documented that Aβ exerts neurotoxic effects and disrupts synaptic structure and functions including spine density decrease, synapse loss and synaptic plasticity impairment[9,10], which may result in memory decline in AD.

Mitogen-activated protein kinase (MAPK) phosphatase 1 (MKP-1), a member of the MKP family, has recently been shown to inactivate MAPK by dephosphorylating MAPK at the tyrosine and threonine residues[11,12]. Previous studies have reported that MKP-1 plays essential roles in neural cell development, survival and death[11,13]. Recently, a study has shown that MKP-1 attenuates apoptosis, oxidative stress and neuroinflammation induced by Aβ through hampering c-Jun N-terminal kinase (JNK) activity in PC12 cells[14], suggesting MKP-1 may exert a neuroprotective role in AD. Indeed, our recent research has found that the expression of MKP-1 is downregulated in the brain tissue of patients and AD model mice, and further reports that upregulation of MKP-1 significantly inhibits the amyloidogenic processing of APP, reduces the senile plaque number and improves cognitive function[15]. Although these findings suggest that MKP-1 plays a vital role in AD pathogenesis, how upstream signaling regulates MKP-1 expression and the molecular mechanisms by which MKP-1 ameliorates AD remain unclear.

MicroRNAs (miRNAs) are small non-coding RNAs that exert their biological functions by directly binding to the 3′ UTR of the mRNAs of protein-coding genes to regulate their expression at the post-transcriptional level[16–18]. In the past decade, several miRNAs that regulate MKP-1 have been reported. For example, miR-101 and let-7b-5p directly target MKP-1 to modulate the activation of MAPK and subsequent production of cytokines in response to inflammatory stimulation[19,20]. *miR-200c* plays a critical role in diabetes-associated cardiac hypertrophy by regulating MKP-1 expression[21]. A recent report shows that *miR-424* protects PC-12 cells from hypoxia-induced injury by directly inhibiting MKP-1 expression[22]. However, little is known about the role of miRNAs in regulating MKP-1 in central nervous system diseases such as AD.

In this study, we found that *miR-429-3p* is abnormally upregulated in the brain of APP23/PS45 double transgenic AD model mice and negatively regulates MKP-1 expression by directly targeting its 3′ UTR. Artificial inhibition of *miR-429-3p* not only suppresses Aβ generation and senile plaque formation but also promotes the surface expression of GluA1-containing AMPARs by regulating the phosphorylation status of GluA1 unit S831 site, thereby alleviating the deficits of synaptic plasticity and spatial learning and memory in AD model mice. Therefore, our results suggest that inhibition of *miR-429-3p* can reduce AD pathology and improve cognitive function by targeting MKP-1.

2. Materials and methods

2.1. Animal

APP23/PS45 double transgenic mice and wild-type (WT) littermates were housed in the experimental animal center of the Children's Hospital of Chongqing Medical University (Chongqing, China). Mice were maintained at controlled temperature and humidity under a 12-h light−dark cycle (lights on 7:00 a.m−7:00 p.m.) and allowed free access to rodent chow and water. All animal experiments were performed with allocation concealment, randomization and blinding. All procedures were performed following Chongqing Science and Technology Commission guidelines for animal research and approved by the Animal Ethics Committee of Chongqing's Hospital of Chongqing Medical University. Every effort was made to minimize both the animal suffering and the number of animals used.

2.2. Antibody and plasmids

C20 (1:1000) synthesized from GL Biochem Ltd. (Shanghai, China) was used to detect APP and CTFs. Anti-MKP-1 (1:1000, #35217), anti-HA-Tag (1:1000, #3724), anti-GluA1 S845 (1:1000, #8084), anti-BACE1 (1:1000, #5606), anti-GluA4 (1:1000, #8070s), anti-p44/42 MAPK (ERK1/2) (1:1000, #4695) and anti-Phospho-p44/42 MAPK (ERK1/2) (1:1000, #4370) antibodies were purchased from CST (Boston, USA). Anti-β-actin (1:3000, #A5411) antibody was obtained from Sigma (St. Louis, MO, USA).

Anti-GluA1 (1:500, ab109450), anti-GluA1 S831 (1:1000, ab109464), anti-GluA2 (1:1000, ab133477), anti-GluA3 (1:1000, ab40845), anti-GFAP (1:1000, ab279291), anti-NeuN (1:500, ab104224), anti-PS1 (1:1000, ab76083) and anti-alpha sodium potassium ATPs (ATPA1) (1:1000, ab7671) antibodies were purchased from Abcam (Cambridge, Cambs, Britain). Anti-PSD95 antibody (1:1000, MAB1598) was purchased from Millipore (Bedford, MA, USA). Anti-MKP-1 (1:100, #381573) antibody was obtained from ZEN BIO (Chengdu, China) for immunofluorescence. Anti-GluA1 S831 (1:200, ZRB04823) antibody was purchased from Sigma for immunofluorescence. Biotin anti-β-amyloid antibody (clone 4G8) (1:200, #800705) was purchased from BioLegend (San Diego, CA, USA). miRNAs mimics/antagomirs and their scramble controls were purchased from RiboBio (RiboBio Co., Ltd. Guangzhou, China). Mimics and antagomirs were used for cell transfection, and antagomir (A-miR-429) or its scramble control (A-scramble) was used for intranasal administration in AD model mice. *GluA1* (tagged HA) plasmid was amplified from human cDNA and inserted into pcDNA3.1. *GluA1 S831D* (tagged HA) plasmid, GluA1 S831 phosphorylation mimic plasmid with the S831 site mutated from serine to aspartic acid, was constructed by homologous recombination. DNA fragments containing the homologous end sequence and HA tags were amplified from the *GluA1* plasmid using the following primers:

GluA1 S831D-F: 5′CACAGCAAGACATCAACGAAGCCATACGGAC-3′;

GluA1 S831D-R: 5′CGTTGATGTCTTGCTGTGGGATCAAACAAAAA-3′.

2.3. Intranasal administration

Two-month-old APP23/PS45 mice were intranasally delivered with A-miR-429 (1 nmol) or its negative control (A-scramble) by instilling 3 μL into each nostril every 2−3 min (a total of 6 doses). The mouse was held for 20 s until the drug was completely inhaled. The effectiveness of A-miR-429 in bypassing the brain−blood barrier was measured by immunofluorescence. Mice were sacrificed at 24 and 48 h after intranasal administration of Cy3-labeled A-miR-429, respectively. The brains were fixed in 4% paraformaldehyde (PFA) for 48 h at 4 °C and then dehydrated with 30% sucrose solution for 48 h. Subsequently, all brain tissues were embedded with OCT at −80 °C. The Frozen brain tissues were cut into 20-μm thicknesses and imaged under a confocal microscope. Image J software calculated the area fraction occupied by CY3-labeled A-miR-429 in red fluorescence. Cy3-labeled A-miR-429 could be detected in mouse brain 24 h (DG: 0.31 ± 0.05, $P = 0.002$ *vs.* 0 h; CA3: 0.65 ± 0.05, $P = 0.004$ *vs.* 0 h; Cortex: 0.46 ± 0.08, $P = 0.002$ *vs.* 0 h; Supporting Information Fig. S3B) or 48 h (DG: 0.12 ± 0.01, $P = 0.377$ *vs.* 0 h, $P = 0.019$ *vs.* 24 h; CA3: 0.31 ± 0.09, $P = 0.292$ *vs.* 0 h, $P = 0.038$ *vs.* 24 h; Cortex: 0.30 ± 0.04, $P = 0.044$ *vs.* 0 h, $P = 0.184$ *vs.* 24 h; Fig. S3B) after intranasal administration of Cy3-labeled A-miR-429 or A-scramble. Therefore, we chose to deliver A-miR-429 intranasally to mice every two days to minimize the side effects of drug use. All mice were administrated with drugs every two days for 2.5 months. Then, behavioral and electrophysiological experiments were performed to assess cognitive and synaptic functions.

2.4. Preparation of Aβ oligomers

Solid powder of Aβ_{42} peptide was purchased from GL Biochem Ltd. (Shanghai, China). To promote oligomer formation, Aβ_{42} powder (1 mg) was dissolved into 1 mL of hexafluoroisopropanol (HFIP) (Sigma) and placed at room temperature for 1 h, then incubated on ice for 5 min. Subsequently, HFIP was clearly removed by vacuum. The peptide was resuspended to 5 mmol/L with dimethylsulfoxide (DMSO), and diluted into 400 μmol/L with Dulbecco's modified Eagle's media/F-12 and then incubated at 4 °C for 48 h. The harvest supernatant was stored at −20 °C or centrifuged at 12,000 rpm (RWD, Shenzhen, China) for 20 min before use.

2.5. Cell culture and transfection

All cells were cultured at 37 °C in a 5% CO_2 atmosphere. N2A (murine neuroblastoma cells) cells were grown in 47% Opti-MEM (Gibco, New York, USA) and 47% DMEM medium, containing 1% streptomycin and 5% fetal bovine serum (FBS). N2A^{APP} cells, N2A stably expressing human Swedish mutant APP695 cells, were cultured in DMEM containing 10% FBS and G418 (100 μg/mL).

To construct *Mkp-1* knock-out (KO) stable cell lines, CRISPR/Cas9 system was introduced. Briefly, a *sgRNA* targeting exon 1 of *Mkp-1* gene was designed using the CRISPR Design tool from Zhang's Lab[23]. pX458 plasmid cloned with *sgRNA* sequence using oligos (oligo 1: CGCCAAGCGCGACGGCACCC, oligo 2: GGGTGCCGTCGCGCTTGGCG) was transfected into N2A^{APP} cells to generate *Mkp-1* KO (*Mkp-1*$^{-/-}$) cell lines. Twenty-four hours after transfection, *sgRNA/Cas9*-positive cells were screened by using puromycin. Puromycin-resistant cells were then diluted and seeded as single cells in 96-well plates. Single cells were expanded and DNA was extracted for PCR and sequencing (Forward primer: 5′-TCGCGGGCTCAGTGAAC-3′, Reverse primer: 5′-ATACAAAGGTACATATTTTCTCATTAGCACC-3′). The protein level of MKP-1 was measured by Western blot (Fig. 2I).

N2A or N2A^{APP} cells were seeded in the six-well plates or 10-cm dishes until grown to 30%−40% confluence and then transfected with *miR-429-3p* mimics/antagomir or *GluA1-HA/GluA1 S831D-HA* plasmids or their negative controls. The medium was completely changed after 4−6 h of transfection, and the cells were further cultured for 24−48 h.

Primarily cultured neurons were isolated from the hippocampus and cortex of embryonic Days 16−19 (E16−19) fetal mice as described previously[24]. In brief, the meninges-free cortex and hippocampus were cut into small pieces and digested with 0.25% trypsin-EDTA. After being digested into single-cell suspension, neuronal cells were plated into a culture plate coated by poly-lysine in DMEM with 10% FBS. After 4−6 h, the medium would be fully replaced by Neurobasal containing 2% B27 supplement and 2 mmol/L glutamine. The medium was half-changed every 3 days. Eight or nine days later, neurons were transfected with *miR-429-3p* antagomir or its control antagomir. Six hours after transfection, the medium was replaced with the fresh medium. Twenty-four hours later, the cells were exposed to 10 μmol/L Aβ_{42} for 24 h. Neurons were used for electrophysiological recording or harvested for Western blotting.

2.6. mRNA extraction and quantitative real-time PCR

Total mRNAs were extracted from tissues and cells using ice-cold Biozol regent (Hangzhou Bori Technology Co., Ltd., China). The total RNA concentration and purity were measured with a spectrophotometer NanoDrop 2000 (Nanodrop Technologies, Wilmington, DE, USA). For single-step synthesis of miRNA

cDNA, the poly(A) polymerase was used to add the poly(A) tails to the 3′ ends of the miRNAs, and the poly(A) miRNAs were reverse transcribed using M-MLV reverse transcriptase and unique oligo (dT) adapter primer. Then, the cDNAs were analyzed by quantitative real-time PCR using 2 × All-in-One qPCR Mix (GeneCopoeia, USA) with the CFX Manager software detection system (Bio-Rad, USA). For the first-strand cDNA synthesis of mRNA, PrimeScript RT reagent Kit (TAKARA, Japan) was used and quantitative RT-PCR was performed using SYBR FAST qPCR Master (KAPA, USA). All primers of miRNAs and RNU6A (*u6*) were purchased from GeneCopoeia Inc. (Rockville, MD, USA). Primer sequences were as follows: *Mkp-1* (Forward primer: 5′-GTACATAAGTCCATCTGAC-3′, Reverse primer: 5′-GGTT CTTCTAGGAGTAGACA-3′); *Gapdh* (Forward primer: 5′-AACT GCTTAGCACCCCTGGC-3′, Reverse primer: 5′-ATGACCT TG CCCACAGCCTT-3′).

2.7. Membrane fractionation in cultured cells

According to the manufacture's protocol, membrane proteins were isolated from cultured cells using a membrane protein extraction kit (Invent Biotechnologies, USA). Briefly, cells were washed 3 times with PBS and resuspended with buffer A containing protease inhibitor cocktail. After incubation in ice for 5 min and vortexing strongly for 10−30 s, the samples were transferred to the columns and centrifuged at 16,000 × *g* (RWD, Shenzhen, China) for 30 s at 4 °C. The columns were then discarded, and the samples were centrifuged at 700 × *g* for 1 min to obtain the supernatant, which was then centrifuged at 16,000 × *g* for 20 min at 4 °C. The pellet was membrane fraction, and was solubilized with minute denaturing protein solubilization reagent (Invent, USA).

2.8. Synaptic fractionation in hippocampal tissues

The synaptic proteins from hippocampal tissue were isolated using a synaptic protein extraction reagent (Thermo Fisher Scientific, USA). Briefly, hippocampal tissues were homogenized with synaptic protein extraction reagent containing the protease inhibitor cocktail (Roche, Switzerland). Then the homogenate was centrifuged at 1200 × *g* for 10 min at 4 °C to obtain the supernatant, which was then centrifuged at 15,000 × *g* for 20 min at 4 °C. The sediments were the synaptic proteins, which were resuspended with synaptic protein extraction reagent.

2.9. Luciferase activity assay

A dual luciferase reporter assay was performed in N2A and $N2A^{APP}$ cells, and the reporter plasmids were purchased from Changsha Youze Biotechnology Co., Ltd. (Changsha, China). The wild-type and mutant-type sequences of *Mkp-1* 3′UTR were synthesized and cloned into the dual-luciferase reporter plasmid psiCHECK, which contains a firefly luciferase (Fluc) reference gene and a *Renilla* luciferase (Rluc) reporter gene. For the luciferase reporter assay, N2A or $N2A^{APP}$ cells were cultured in 48-well plates and co-transfected with the wild-type or mutant *Mkp-1* 3′UTR reporter plasmids and *miRNA-429-3p* mimics or A-miR-429 or its negative controls with Lipofectamine 3000 according to the manufacturer's protocol. Forty-eight hours later, the cells were harvested, and lysates were used for detecting Firefly and *Renilla* luciferase activities with the dual luciferase reporter assay kit (Promega, Wisconsin, USA) according to manufacturer's protocol.

2.10. Barnes maze test

The apparatus of the Barnes maze test includes a white circular platform (0.75 m in diameter) with 18 holes (5 cm in diameter) in the edges and an escape box under one of these holes. A CCD camera records the tracking events, and an ANY-maze video tracking system (Stoelting, USA) is used to analyze the records and obtain latency and count of errors of finding the escape box. The Barnes maze test contains three phases: an adaptive phase, an acquisition phase and a probe test. In the adaptive phase (Day 0), all mice were given 3 min to adapt to the maze before the acquisition phase. During the acquisition phase (Days 1−5), mice were trained in spatial learning tasks for 2 trials per day. In each trial, mice were placed in the center of the platform and the latency of entering the escape box was recorded. If the animal could find and enter the escape box within 3 min, the animal would be put back to its home cage. If the animal couldn't find the escape box or could find but didn't enter the escape box within 3 min, it would be gently guided to find and enter the box and stay 60 s before being put back in its cage. Twenty-four hours after the last learning trial, a probe test (Day 6) was performed with the escape box moved away for 3 min.

2.11. Morris water maze test

The Morris water maze consisted of a circular stainless steel pool (150 cm in diameter) filled with water (25 ± 1 °C) made opaque with nontoxic white paint. The pool was surrounded by light blue curtains, and 3 distal visual cues were fixed to the curtains. The Morris water maze test contains three phases: an adaptive phase, acquisition phase and probe test. Twenty-four hours before spatial training (Day 0), the mice were given 120 s to swim freely to adapt the maze. During the acquisition phase (Days 1−5), all mice were trained in spatial learning tasks for 4 trials per day. In each trail, mice were put into water from 4 starting positions (NE, NW, SW, SE), facing the pool water. A CCD was used to record the tracks of swim and the latency to find the hidden platform submerged in 1 cm of opaque water surface. During each trial, mice were allowed to swim until they found the platform where they should stay for 20 s. If mice failed to find the platform within 120 s, the mice would be guided to the platform and stay for 20 s. Twenty-four hours after the training, a probe test (Day 6) was performed from a novel drop point with the hidden platform absent for 120 s.

2.12. Open field test

Mice were placed in the center of the open field, a clear plastic box (42 cm × 42 cm × 42 cm), to freely explore for 10 min. The total travel distance was recorded using the ANY-maze tracking system (Stoelting, USA).

2.13. Tail-suspension test

Mice were suspended by their tails using medical tapes on the metal hook of horizontal rails (45 cm above the floor) and recorded for 5 min by ANY-maze tracking system (Stoelting, USA). Latency to immobility and the total immobility time were recorded.

2.14. Elevated-plus maze test

The apparatus consists of two opposite open arms and two opposite closed arms (20-cm-tall walls on the closed arms) arranged at right angles (each arm 30 cm). During the test, mice were placed in the center of the maze that was elevated 70 cm above the floor. The number of entries and time spent in the open arms were recorded for 5 min by ANY-Maze Video Tracking System (Stoelting, USA).

2.15. Western blot

The cells and brain tissues were lysed with lysis buffer and incubated on ice for 20 min, and then homogenates were centrifuged (4 °C, 12,000 rpm, 20 min) to collect the supernatant. Samples (30 μg for total protein and 15 μg for membrane or synaptic fractionation) were boiled with the protein sample loading buffer (Epizyme, Shanghai, China) at 95 °C for 10 min. The samples were separated on 12.5% tris-glycine SDS-PAGE or 16% tris-tricine SDS-PAGE gels and then transferred onto polyvinylidene difluoride (PVDF) membranes (Bio-Rad, USA). After blocking with 5% nonfat milk, the membranes were rinsed with TBS and 0.1% Tween (TBST) for 5 min. Then, the membranes were incubated in primary antibody overnight at 4 °C. The membranes were washed with TBST 3 times, 5 min each time, and then were incubated in secondary antibody for 1.5 h at room temperature. The membranes were washed with TBST 3 times again, 5 min each. After removing the TBST, the blot was developed with Western ECL Substrate (Bio-Rad) and imaged with BIO-RAD Imager System (USA). The gray values of Western bands were analyzed quantitatively by Quantity One software. An Odyssey Imaging System (Licor, USA) was introduced to quantify fluorescence intensity when IRDye 800C secondary antibody (1:5000, 926-32211, Licor, USA) and IRDye 680LT secondary antibody (1:5000, 925-68020, Licor, USA) were used.

2.16. Immunohistochemistry and immunofluorescence

After the behavioral test, the mice were deeply anesthetized with urethane. Half of the brain was fixed in freshly 4% PFA for 48 h at 4 °C, and then dehydrated by placing it into 30% sucrose for 48 h, embedded with optimal cutting temperature compound (OCT) at −80 °C. To detect the plaques, immunohistochemistry was performed. In brief, the brains were sectioned into 30-μm brain slices with Leica Cryostat (CM1850, Leica, Germany). To eliminate residual peroxidase activity, the brain slices were incubated in 3% H_2O_2 for 30 min. Subsequently, the slices were blocked with 10% bovine serum albumin for 1 h and incubated 4G8 antibody overnight at 4 °C. Every sixth slice with the same reference position was mounted onto slides for staining. Immunocytochemical staining was performed on floating sections. Plaques were detected by the ABC and DAB kit and all strained slides were scanned using a whole-slide scanner (Olympus, Japan). Plaques were quantitated, and the mean plaque count in the hippocampus was recorded for each mouse as described previously[25]. The area of senile plaque was calculated using Image J software.

To detect the expression of MKP-1 in the brain of mice, the immunofluorescent assay was performed. The brains were sectioned into 20-μm brain slices with Leica Cryostat. The slices were washed with PBS three times for 5 min each and then blocked with immunofluorescence sealing fluid for 1 h at room temperature. Subsequently, the brain slices were incubated with primary antibody at 4 °C overnight. After washing with PBST, slices were incubated with goat anti-rabbit and goat anti-rabbit secondary antibodies conjugated to Alexa Fluor dyes and DNA strain 4,6-diamidino-2-phenylindole (DAPI). Then slices were washed with PBS containing 0.05% Twen-20 and were mounted on the slides with an antifade mounting medium. Immunofluorescent images were acquired using a confocal microscope.

2.17. miRNAscope

The expression of *miR-429-3p* was investigated by using the miRNAscope HD Detection Kit (Advanced Cell Diagnostics [ACD], USA) according to the manufacturer's protocol. In brief, a 20-μm-thick frozen section of mouse brain was pretreated and hybridized with ZZ-probe (Probe-SR-mmu-miR-429-3p-S1, ACD) targeting *miR-429-3p* for 2 h at 40 °C. The ZZ-pairs binding *miR-429-3p* were detected by using six amplification steps before visualized with Fat Red. Then DAPI was used to stain nucleic acids. Images were acquired by using a confocal microscope.

2.18. Electrophysiological recording

The primary cultured neurons were used for electrophysiological recordings between 10 and 12 days after plating. Cultured neurons were transfected with A-miR-429 or A-scramble on Day 8 of plating and treated with Aβ (10 μmol/L) for 24 h before electrophysiological recording. Whole cell patch-clamp recordings were performed at room temperature using a HEKA EPC 10 amplifier (HEKA, Germany) and PatchMaster software (filtered at 3 kHz and sampled at 10 kHz). Whole-cell recording pipettes (3−5 MΩ) were filled with a solution containing (mmol/L): CsCL 140, HEPES10, Mg-ATP 4, QX-314 5, pH 7.2 and 290−295 mOsm. The cultured neurons were incubated in the extracellular solution containing (mmol/L): NaCl 140, KCl 5.4, HEPES 10, $MgCl_2$ 1.0, $CaCl_2$ 1.3, glucose 20, pH 7.4; osmolarity, 305−315 mOsm. For a recording of miniature excitatory postsynaptic currents (mEPSCs), TTX (1 mmol/L) and PTX (100 μmol/L) were added into extracellular solution to minimize the activation of NMDAR and voltage-gated sodium channels, respectively. mEPSC were recorded at a holding potential of −70 mV. The frequency and amplitude of mEPSCs were quantified by Mini Analysis Program 6.0.3 (Synaptosoft Inc., Decatur, GA, USA).

For long-term potentiation (LTP) recording, the field excitatory postsynaptic potentials (fEPSPs) were made from the CA1 stratum radiatum of the hippocampus in response to stimulation of the Schaffer collateral/commissural pathway. In brief, mice were deeply anesthetized with urethane (1.5 g/kg, i.p.) and cardiacally perfused with artificial cerebral spinal fluid (ACSF) (in mmol/L: NaCl 124, KCl 2.8, $NaH_2PO_4.H_2O$ 1.25, $CaCl_2$ 2.0, $MgSO_4$ 1.2, Na-vitamin C 0.4, Na-lactate 2.0, Na-pyruvate 2.0 and D-glucose 10.0, pH = 7.4). After decapitation, the brain was rapidly removed and submerged in ice-cold ACSF oxygenated with 95% O_2 and 5% CO_2. Then, brain slices were coronally sectioned (400 μm) with vibratome (VT1200S, Leica Microsystems, Bannockburn, IL, USA) and incubated in ACSF (95% O_2 and 5% CO_2) for 2 h at 35 °C. A bipolar stimulating electrode was placed at the Schaffer collaterals of dorsal hippocampus CA3 pyramidal neurons, and a recording pipette filled with ASCF was placed at the ipsilateral striatum radiatum of the hippocampal CA1 area. Test EPSCs were evoked at a frequency of 0.05 Hz and at a stimulus intensity adjusted to 50% of the maximal response. After

a 30-min stable baseline, theta burst stimulation (TBS) was given to induce LTP. TBS contained 2 trains of stimuli (at 20 s interval), and each train contained 5 bursts (4 pulses at 100 Hz in each burst) at an inter-burst interval of 200 ms.

2.19. Statistical analysis

All data were expressed as mean ± standard error of mean (SEM) and analyzed using SPSS. The training data of Barnes maze and water maze were analyzed by a two-way between/within-subjects factorial ANOVA, with drug treatment as the between-subjects factor and training session (time) as the within-subjects factor. All significant main effects and interactions were further analyzed using Turkey's comparisons. Other data were analyzed by a one-way between-subjects factorial ANOVA or two-tailed student's *t* tests where appropriate. All experiments were performed three times and the significance level was set at $P < 0.05$.

3. Results

3.1. The expression of miR-429-3p is abnormally increased and inhibits MKP-1 expression by directly targeting MKP-1 in AD

Our recent study has reported that MKP-1 is downregulated in the brain of AD model mice and in AD model cells[15]. We here first confirmed that the protein levels of MKP-1 were reduced in the cortex ($n = 5$, 0.29 ± 0.08, $P = 0.012$ *vs.* WT; Supporting Information Fig. S1A) and hippocampus ($n = 4$, 0.59 ± 0.10, $P = 0.021$ *vs.* WT; Fig. S1B) of APP/PS45 mice, and in N2A^{APP} cells ($n = 10$, 0.52 ± 0.06, $P = 0.004$ *vs.* N2A; Fig. S1C). Growing evidence indicates that miRNAs negatively regulate gene expression by binding to the 3′UTR of mRNA to repress translation and/or degrade mRNA[26]. *Mkp-1* contains a long 3′UTR (1875 nt), suggesting a possible negative regulation by miRNAs. To understand the potential miRNAs in regulating MKP-1 expression, we performed a systematic analysis to predict *Mkp-1* expression-related miRNAs by TargetScan, and several miRNAs including *miR-429-3p*, *miR-200b/c-3p*, *miR-101a/b-3p*, *miR-137-3p*, *miR-152-3p*, *miR-92a-3p*, *miR-133a/b-3p* and *miR-133c* were predicted to target *Mkp-1* (Supporting Information Fig. S2A). We next performed qRT-PCR to measure the expression profile of MKP-1 expression-related miRNAs in the brain of AD model mice. We found that the *miR-429-3p*, *miR-200b-3p* and *miR-200c-3p* were significantly higher in AD model mice compared with the WT littermates (Fig. 1A). However, only an increase in *miR-429-3p* ($n = 5$−6, 1.78 ± 0.15, $P = 0.026$ *vs.* N2A; Fig. 1B), but not in *miR-200b-3p* ($n = 3$, 1.03 ± 0.38, $P = 0.953$ *vs.* N2A; Fig. S2C) and *miR-200c-3p* ($n = 5$, 1.66 ± 0.38, $P = 0.159$ *vs.* N2A; Fig. S2D), was observed in N2A^{APP} cells compared with N2A cells. An increase in *miR-429-3p* was also observed in primarily cultured neurons treated with Aβ_{42} ($n = 3$−5, 2.38 ± 0.38, $P = 0.036$ *vs.* Ctrl; Fig. 1C).

As shown in Fig. 1D, the level of *miR-429-3p* was significantly elevated in the N2A cells transfected *miR-429-3p* (*miR-429-3p* group: $n = 3$, 385.59 ± 88.66, $P = 0.012$ *vs.* Scramble group, Fig. 1D). To investigate whether *Mkp-1* is the direct target of these miRNAs, the luciferase reporter assay was performed. The results showed that overexpression of *miR-429-3p* significantly inhibited the reporter activity of WT *Mkp-1* 3′ UTR (WT + *miR-429-3p*: $n = 3$, 0.60 ± 0.05, $P = 0.030$ *vs.* WT + Scramble; Mut + *miR-429-3p*: $n = 3$, 1.01 ± 0.13, $P = 0.520$ *vs.* Mut + Scramble; Fig. 1E), but not mutant (Mut) *Mkp-1* 3′ UTR in N2A cells. Overexpression of *miR-200b-3p* (WT + *miR-200b-3*p: $n = 5$, 0.65 ± 0.05, $P = 0.001$ *vs.* WT + Scramble; Mut + *miR-200b-3p*: $n = 5$, 1.08 ± 0.04, $P = 0.240$ *vs.* Mut + Scramble; Fig. S2E) or *miR-200c-3p* (WT + *miR-200c-3p*: $n = 5$, 0.51 ± 0.03, $P < 0.001$ *vs.* WT + Scramble; Mut + *miR-200c-3p*: 0.98 ± 0.01, $n = 5$, $P = 0.861$ *vs.* Mut + Scramble; Fig. S2F), similar to the *miR-429-3p*, also inhibited the reporter activity of WT *Mkp-1* 3′UTR. To elucidate whether these miRNAs can regulate the protein level of MKP-1, we then transfected miRNA mimics into N2A cells. The results showed that overexpression of *miR-429-3p* ($n = 4$, 0.68 ± 0.02, $P = 0.023$ *vs.* Scramble; Fig. 1G), but not *miR-200b-3p* ($n = 6$, 1.06 ± 0.04, $P = 0.641$ *vs.* Scramble; Fig. S2G) or *miR-200c-3p* ($n = 6$, 1.02 ± 0.09, $P = 0.937$ *vs.* Scramble; Fig. S2H), significantly reduced the level of MKP-1 protein. Meanwhile, *miR-429-3p* did not alter *Mkp*-1 mRNA level ($n = 3$, 0.88 ± 0.20, $P = 0.689$ *vs.* Scramble; Fig. 1F) and the sequence was highly conserved across species (Fig. S2B). To further detect the role of these miRNAs in regulating MKP-1 in AD, either antagomir of miRNA or antagomir-negative control was transfected into the N2A^{APP} cells. The results showed that antagomir of *miR-429-3p* (A-miR-429), which did not affect the expression of *miR-429-3p* ($n = 5$, 1.31 ± 0.40, $P = 0.511$ *vs.* A-scramble; Fig. 1H), was able to upregulate MKP-1 protein expression compared with its control (A-scramble) ($n = 4$, 1.75 ± 0.10, $P = 0.020$ *vs.* A-scramble; Fig. 1I). However, antagomirs of both *miR-200b-3p* (A-miR-200b: $n = 4$, 1.11 ± 0.26, $P = 0.719$ *vs.* A-scramble; Fig. S2I) and *miR-200c-3p* (A-miR-200c: $n = 4$, 0.91 ± 0.26, $P = 0.806$ *vs.* A-scramble; Fig. S2J) had no influence on MKP-1 protein expression. Consistent with our previous findings, A-miR-429 markedly increased the luciferase activity of WT *Mkp-1* 3′UTR had reporter to 1.49 ± 0.11 ($n = 3$, $P = 0.032$ *vs.* WT + A-scramble; Fig. 1J), but not Mut 3′UTR (Mut + A-miR-429: 1.05 ± 0.16, $P = 0.552$ *vs.* Mut + A-scramble; Fig. 1J) in N2A^{APP} cells. Collectively, although several miRNAs are predicted to directly target *Mkp-1*, only *miR-429-3p* can directly target *Mkp*-1 mRNA to suppress its translation. We therefore mainly focused on the possible role of *miR-429-3p* in AD in the present study.

3.2. Inhibition of miR-429-3p reduces APP amyloidogenic processing

To determine whether *miR-429-3p* affects APP processing, N2A cells were transfected with *miR-429-3p* mimics. We found that overexpression of *miR-429-3p* upregulated the protein levels of APP ($n = 6$, 1.63 ± 0.19, $P = 0.041$ *vs.* Scramble; Fig. 2A and B) and PS1 ($n = 6$, 1.46 ± 0.14, $P = 0.025$ *vs.* Scramble; Fig. 2A and D), but did not affect the protein level of BACE1 ($n = 6$, 1.04 ± 0.17, $P = 0.851$ *vs.* Scramble; Fig. 2A and C) in comparison with its scramble control. Then, the *miR-429-3p* antagomir (A-miR-429) was transfected into the N2A^{APP} cells to further assess the effect of *miR-429-3p* inhibition on APP processing in AD. The efficiency of A-miR-429 transfection into N2A^{APP} cells was indicated by the red fluorescence intensity (Cy3-A-miR-429: 34.34 ± 8.53, $n = 3$−4, $P = 0.034$ *vs.* Ctrl; Supporting Information Fig. S3A). The results showed that A-miR-429 transfection downregulated the protein levels of APP ($n = 5$, 0.74 ± 0.08, $P = 0.038$ *vs.* A-scramble; Fig. 2E and F), BACE1 ($n = 6$, 0.66 ± 0.10, $P = 0.018$ *vs.* A-scramble; Fig. 2E and G) and PS1 ($n = 6$, 0.72 ± 0.06, $P = 0.038$ *vs.* A-scramble; Fig. 2E and H). To further verify the effect of A-miR-429 in APP processing, we

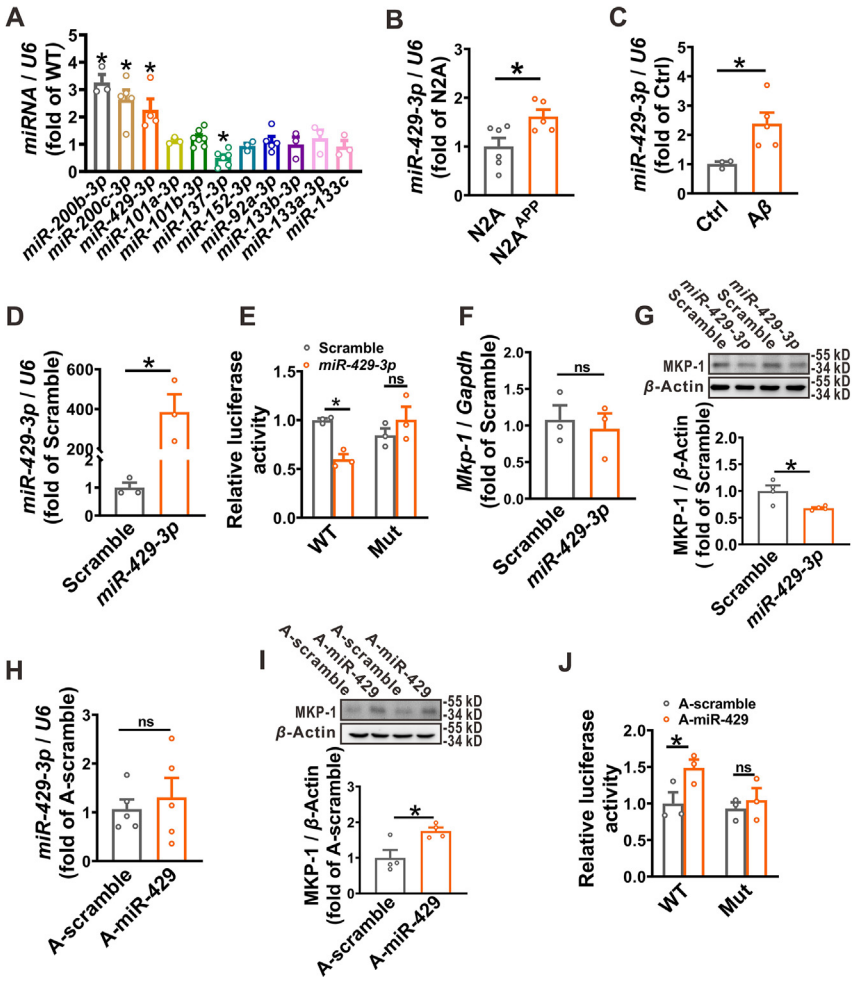

Figure 1 The *miR-429-3p* is abnormally increased and inhibits MKP-1 expression by directly binding to *Mkp*-1 mRNA. (A) The expression of several miRNAs targeting 3′UTR of *Mkp-1* in brain tissues of APP23/PS45 and WT mice (n = 3−7). (B)−(C) The expressions of *miR-429-3p* in N2A and N2A^{APP} cells (B), in primarily cultured neurons treated with Aβ_{42} (10 μmol/L) for 24 h (C), and in N2A cells transfected with *miR-429-3p* or its control scramble (D) (n = 3−6). (E) Relative luciferase activity is assessed in the N2A cells co-transfected with *miR-429-3p* or its control scramble and plasmids containing WT or mutant (Mut) 3′UTR of *Mkp-1* (n = 3). (F)−(G) The expression of *Mkp*-1 mRNA (F) and protein (G) is assessed in N2A cells transfected *miR-429-3p* or its scramble control (n = 3−5). (H)−(I) The expression of *miR-429-3p* (H) and MKP-1 protein (I) in N_2A^{APP} cells transfected with A-miR-429 or A-scramble (n = 4−5). (J) Relative luciferase activity is assessed in N_2A^{APP} cells co-transfected plasmids containing WT or mutant (Mut) 3′UTR of *Mkp-1* and A-miR-429 or its scramble control (n = 3). Data are expressed as mean ± SEM. ns, not significant; *P < 0.05.

constructed *Mkp-1*$^{-/-}$ cell lines in N2A^{APP} cells by CRISPR/Cas9 system (Fig. 2I). The results showed that A-miR-429 could not change the protein levels of APP (n = 4, 1.08 ± 0.23, P = 0.816 *vs.* A-scramble; Fig. 2J and K), BACE1 (n = 5, 0.93 ± 0.07, P = 0.675 *vs.* A-scramble; Fig. 2J and L), and PS1 (n = 5, 1.04 ± 0.15, P = 0.873 *vs.* A-scramble; Fig. 2J and M) in *Mkp-1*$^{-/-}$ cells.

To further elucidate the role of *miR-429-3p* in AD pathogenesis *in vivo*, we generated Cy3-labeled A-miR-429, a chemically modified stabilized antagomir complementary to *miR-429-3p* that inhibits endogenous *miR-429-3p* function and can easily cross the blood−brain barrier (Fig. S3B). We first detected the effect of A-miR-429 on the expression of *miR-429-3p* in AD model mice by using miRNAscope assay. The results showed that the level of *miR-429-3p* was increased, while A-miR-429 reduced its expression in AD model mice (Fig. 2N). The immunofluorescent imaging assay showed the protein level of MKP-1 was significantly decreased in the neurons (Fig. 2O) rather than astrocytes (Fig. S3C) of AD model mice, and inhibition of *miR-429-3p* by A-miR-429 was able to rescue its expression. Similar to the finding in N2A^{APP} cells, A-miR-429 treatment could restore the expression of MKP-1 to control level in the brains of AD model mice (n = 4; AD + A-scramble: 0.64 ± 0.05, P = 0.049 *vs.* WT + A-scramble; AD + A-miR-429: 1.04 ± 0.11, P = 0.031 *vs.* AD + A-scramble, P = 0.951 *vs.* WT + A-scramble; Fig. 2P and Q). In addition, A-miR-429 treatment led to a marked reduction in the levels of BACE1 (n = 4; AD + A-scramble: 1.69 ± 0.07, P = 0.002 *vs.* WT + A-scramble; AD + A-miR-429: 1.07 ± 0.12, P = 0.004 *vs.* AD + A-scramble, P = 0.869 *vs.* WT + A-scramble; Fig. 2P and R) and CTF (n = 8; AD + A-scramble: 35.94 ± 3.52, P < 0.001 *vs.* WT + A-scramble; AD + A-miR-429: 24.34 ± 3.11, P = 0.017 *vs.* AD + A-scramble, P < 0.001 *vs.* WT + A-scramble; Fig. 2P and S), but not APP (n = 4; AD + A-scramble: 2.04 ± 0.10, P < 0.001 *vs.* WT + A-scramble;

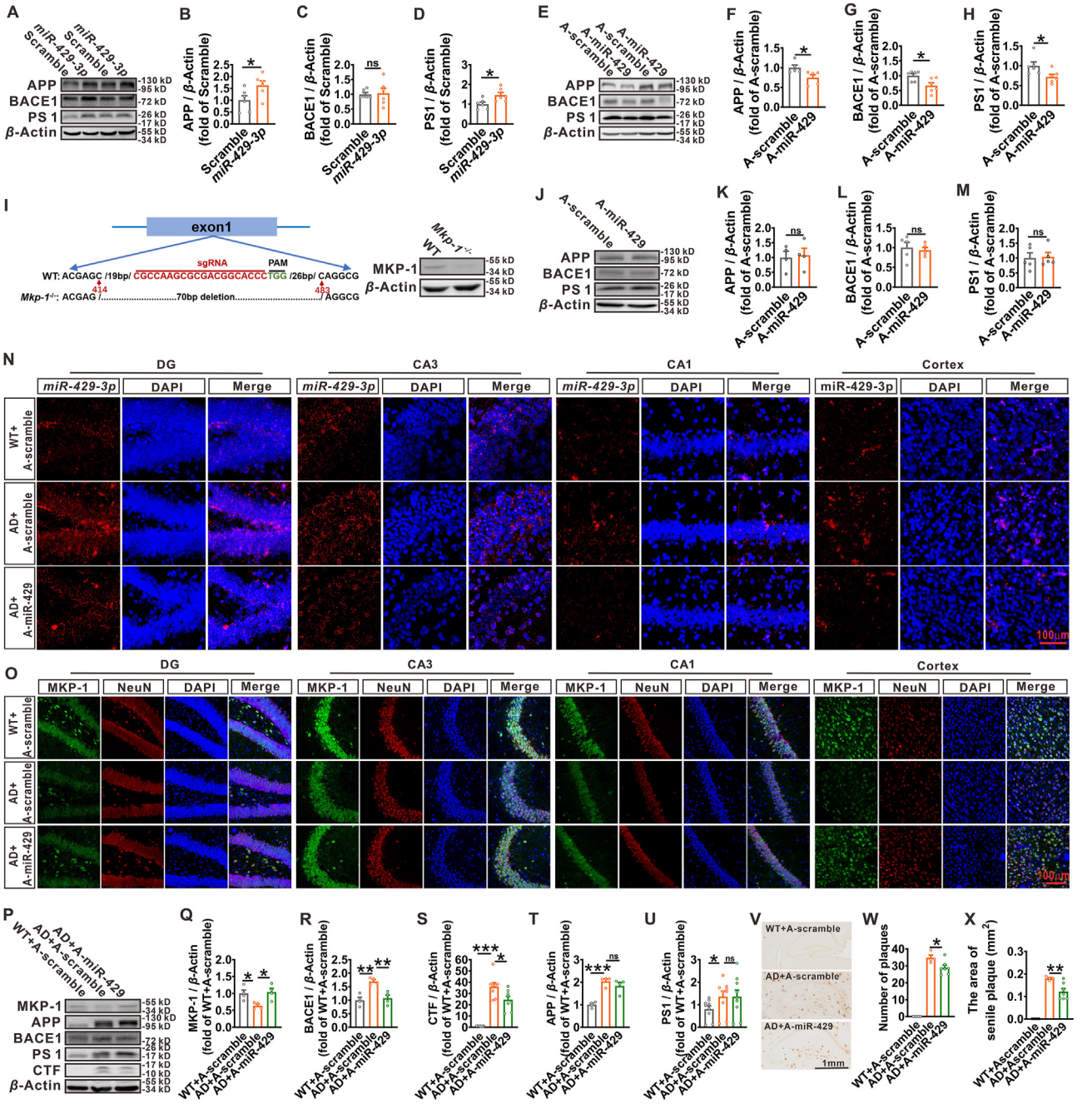

Figure 2 Effects of *miR-429-3p* on APP amyloidogenic processing. (A)−(D) Protein levels of APP (B), BACE1 (C) and PS1 (D) in N_2A cells transfected with *miR-429-3p* or its scramble control (Scramble) ($n = 6$). (E)−(H) The relative protein levels of APP (F), BACE1 (G) and PS1 (H) are assessed by Western blot in N_2A^{APP} cells transfected with A-miR-429 or A-scramble ($n = 5$−6). (I) Genomic DNA sequences of *Mkp-1* locus in *Mkp-1*$^{-/-}$ $N2A^{APP}$ cells, and the protein level of MKP-1 in WT and *Mkp-1*$^{-/-}$ cells ($n = 3$). (J)−(M) The protein levels of APP (K), BACE1 (L), and PS1 (M) in *Mkp-1*$^{-/-}$ cells transfected with A-miR-429 or A-scramble ($n = 4$−5). (N) The expression of *miR-429-3p* is assessed by miRNAscope in the brain slices of APP23/PS45 mice treated with A-miR-429 or A-scramble, Scale bar, 100 μm. (O) Immunofluorescent staining for MKP-1 (green) and neuronal marker NueN (red) in the different brain regions of APP23/PS45 mice treated with A-miR-429 or A-scramble, Scale bar, 100 μm. (P)−(U) Protein levels of MKP-1 (Q), BACE1 (R), CTF (S), APP (T) and PS1 (U) in APP23/PS45 mice treated with A-miR-429 or A-scramble ($n = 4$−8). (V)−(X) The number (W) and the area (X) of senile plaques are detected by immunohistochemistry in the hippocampus of APP23/PS45 mice treated with A-miR-429 or A-scramble ($n = 46$−70 slices from 4 to 7 mice), Scale bar, 1 mm. Data are expressed as mean ± SEM. ns, not significant; $^*P < 0.05$, $^{**}P < 0.01$, $^{***}P < 0.001$.

AD + A-miR-429: 1.84 ± 0.15, $P = 0.432$ *vs.* AD + A-scramble, $P = 0.001$ *vs.* WT + A-scramble; Fig. 2P and T) and PS1 ($n = 7$; AD + A-scramble: 1.69 ± 0.14, $P = 0.030$ *vs.* WT + A-scramble; AD + A-miR-429: 1.70 ± 0.25, $P = 0.999$ *vs.* AD + A-scramble, $P = 0.027$ *vs.* WT + A-scramble; Fig. 2P and U) in the brain of AD model mice. To determine whether *miR-429-3p* affects the AD-related neuropathologies, the formation of senile plaques was examined. A-miR-429 treatment significantly reduced the number

of senile plaques in the hippocampus of AD model mice (WT + A-scramble: $n = 70$ slices from 5 mice; AD + A-scramble: $n = 46$ slices from 4 mice, 34.80 ± 1.57, $P < 0.001$ *vs.* WT + A-scramble; AD + A-miR-429: $n = 60$ slices from 7 mice, 28.90 ± 1.50, $P = 0.024$ *vs.* AD + A-scramble, $P < 0.001$ *vs.* WT + A-scramble; Fig. 2V and W). In addition to the number of plaques, the senile plaque area was also significantly reduced in the hippocampus of AD model mice treated with A-miR-429 (WT + A-scramble: $n = 70$ slices from 5 mice; AD + A-scramble: $n = 46$ slices from 4 mice, 0.18 ± 0.01 mm^2, $P < 0.001$ *vs.* WT + A-scramble; AD + A-miR-429: $n = 60$ slices from 7 mice, 0.12 ± 0.01 mm^2, $P = 0.008$ *vs.* AD + A-scramble; $P < 0.001$ *vs.* WT + A-scramble; Fig. 2V and X). Collectively, these results demonstrate that A-miR-429 inhibits APP amyloidogenic processing and senile plaque formation in the APP23/PS45 AD model mice.

3.3. *Inhibition of miR-429-3p increases surface GluA1 through decreasing GluA1 S831 hyperphosphorylation*

Given that our recent study has documented that MKP-1 ameliorates the cognitive decline and synaptic plasticity in AD model mice[15], and AMPAR trafficking and distribution play critical roles in mediating LTP[25,27,28], we next wanted to detect the effect of A-miR-429 on the expressions of AMPAR subunits including GluA1, GluA2, GluA3 and GluA4. The results showed that A-miR-429 did not affect the expressions of total GluA1 ($n = 7$; AD + A-scramble: 0.93 ± 0.12, $P = 0.971$ *vs.* WT + A-scramble; AD + A-miR-429: 1.45 ± 0.30, $P = 0.257$ *vs.* AD + A-scramble, $P = 0.359$ *vs.* WT + A-scramble; Fig. 3A and B), GluA2 ($n = 7$; AD + A-scramble: 1.03 ± 0.12, $P = 0.987$ *vs.* WT + A-scramble; AD + A-miR-429: 0.97 ± 0.12, $P = 0.947$ *vs.* AD + A-scramble, $P = 0.987$ *vs.* WT + A-scramble; Fig. 3A and C), GluA3 (AD + A-scramble: $n = 7$, 1.07 ± 0.15, $P = 0.909$ *vs.* WT + A-scramble; AD + A-miR-429: 1.21 ± 0.11, $n = 7$, $P = 0.468$ *vs.* WT + A-scramble, $P = 0.718$ *vs.* AD + A-scramble; Fig. 3A and D) and GluA4 (AD + A-scramble: $n = 6$, 1.27 ± 0.42, $P = 0.852$ *vs.* WT + A-scramble; AD + A-miR-429: 1.71 ± 0.43, $n = 6$, $P = 0.359$ *vs.* WT + A-scramble, $P = 0.666$ *vs.* AD + A-scramble; Fig. 3A and E) in the total tissue lysates of brain tissues collected from 4.5-month-old AD model mice. However, the protein levels of GluA1 ($n = 6$; AD + A-scramble: 0.71 ± 0.08, $P = 0.044$ *vs.* WT + A-scramble; Fig. 3F and G) and GluA2 ($n = 6$; AD + A-scramble: 0.63 ± 0.07, $P = 0.024$ *vs.* WT + A-scramble; Fig. 3F and H) was markedly decreased in the hippocampal synaptic fraction of AD mice compared with WT, whereas A-miR-429 restored the protein expression of synaptic GluA1 ($n = 6$; AD + A-miR-429: 1.01 ± 0.09, $P = 0.038$ *vs.* AD + A-scramble, $P = 0.943$ *vs.* WT + A-scramble; Fig. 3F and G, but not GluA2 ($n = 6$; AD + A-miR-429: 0.81 ± 0.11, $P = 0.250$ *vs.* AD + A-scramble, $P = 0.212$ *vs.* WT + A-scramble; Fig. 3F and H), to WT level. Notably, the protein levels of GluA3 (AD + A-scramble: $n = 4$, 1.07 ± 0.06, $P = 0.854$ *vs.* WT + A-scramble; AD + A-miR-429: 1.26 ± 0.10, $n = 4$, $P = 0.135$ *vs.* WT + A-scramble, $P = 0.291$ *vs.* AD + A-scramble; Fig. 3F and I) and GluA4 (AD + A-scramble: $n = 4$, 1.00 ± 0.14, $P = 1.000$ *vs.* WT + A-scramble; AD + A-miR-429: 1.03 ± 0.12, $n = 4$, $P = 0.984$ *vs.* WT + A-scramble, $P = 0.981$ *vs.* AD + A-scramble; Fig. 3F and J) in the hippocampal synaptic fractions were no significant difference among three groups.

We next wanted to further determine the underlying mechanism of A-miR-429-mediated increase in surface GluA1. As phosphorylation at S831 and S845 residues of GluA1 plays a crucial role in GluA1 trafficking[29–31], we next examined the effect of A-miR-429 on GluA1 phosphorylation. The results showed that elevated GluA1 S831 phosphorylation (pGluA1 S831) was observed in 4.5-month-age AD model mice ($n = 7$; AD + A-scramble: 1.63 ± 0.24, $P = 0.031$ *vs.* WT + A-scramble; Fig. 3K and L) compared with WT mice, resulting in a significantly increased the ratio of pGluA1 S831 and GluA1 ($n = 5$; AD + A-scramble: 1.64 ± 0.20, $P = 0.030$ *vs.* WT + A-scramble; Fig. 3M). Importantly, A-miR-429 treatment could reduce the level of pGluA1 S831 ($n = 7$; AD + A-miR-429: 1.01 ± 0.20, $P = 0.033$ *vs.* AD + A-scramble, $P = 0.986$ *vs.* WT + A-scramble; Fig. 3K and L) and the ratio of pGluA1 S831 and GluA1 ($n = 5$; AD + A-miR-429: 0.65 ± 0.09, $P = 0.002$ *vs.* AD + A-scramble, $P = 0.276$ *vs.* WT + A-scramble; Fig. 3M) to WT level. However, the phosphorylation of GluA1 S845 (pGluA1 S845) in AD model mice remained unchanged with or without A-miR-429 treatment ($n = 6$; AD + A-scramble: 1.02 ± 0.08, $P = 0.992$ *vs.* WT + A-scramble; AD + A-miR-429: 0.85 ± 0.07, $P = 0.500$ *vs.* AD + A-scramble, $P = 0.571$ *vs.* WT + A-scramble; Fig. 3K and N) compared with WT mice. The immunofluorescent imaging data showed that the expression of GluA1 was no visible change among these three groups (Fig. 3O). However, the expression of pGluA1 S831 was increased in the AD model mice (AD + A-scramble), compared with WT group (WT + A-scramble), and intranasal administration of A-miR-429 (AD + A-miR-429) decreased pGluA1 S831 level compared with its scramble (Fig. 3P), which was consistent with that of Western blot. These findings demonstrate that pGluA1 S831 is enhanced in AD model mice, and inhibition of *miR-429-3p* by A-miR-429 reduces pGluA1 S831 level.

However, previous studies have reported that pGluA1 S831 is required for the GluA1 insertion into the postsynaptic membrane during LTP[30,32,33], but LTP is impaired in AD[34,35]. To clarify these contradictory findings, the brain tissues from 1.5 to 12-month-old AD model mice were collected to analyze the expression of GluA1 and pGluA1 S831. We found that the protein expression of GluA1 was increased in the brains of 3-month-old ($n = 4$, 1.77 ± 0.23, $P = 0.040$ *vs.* WT; Fig. S4E and S4G) and was decreased in 12-month-old ($n = 5$, 0.45 ± 0.10, $P = 0.011$ *vs.* WT; Fig. S4M and S4O) AD model mice, while it remained unchanged in 1.5- (Fig. S4A and S4C), 4.5- (Fig. 3A and B) and 6-month-old (Fig. S4I and S4K) AD model mice compared with WT mice, suggesting that GluA1 protein expression in AD initially increased and then decreased with age (Fig. 3Q). The protein level of pGluA1 S831 was reduced in the brain tissues of 1.5-month-old ($n = 5$, 0.55 ± 0.04, $P = 0.020$ *vs.* WT; Supporting Information Fig. S4A and S4B) AD model mice and was increased in 4.5- (Fig. 3K and L) and 6-month-old ($n = 4$, 1.16 ± 0.06, $P = 0.043$ *vs.* WT; Fig. S4I and S4J) mice, while remained unchanged in 3- (Fig. S4E and S4F) and 12-month-old (Fig. S4M and S4N) AD model mice compared with WT mice, suggesting that pGluA1 S831 protein expression in AD initially decreased and then increased with age (Fig. 3Q). The dynamic changes of GluA1 and pGluA1 S831 led to a gradual increase in the ratio of pGluA1 S831 and total GluA1 with the progression of AD (1.5 months: $n = 5$, 0.45 ± 0.09, $P = 0.041$ *vs.* WT; 3 months: $n = 4$, 0.53 ± 0.06, $P = 0.038$ *vs.* WT; 6 months: $n = 4$, 1.37 ± 0.10, $P = 0.025$ *vs.* WT; 12 months: $n = 5$, 3.00 ± 0.70, $P = 0.045$ *vs.* WT; Fig. S4D, S4H, S4L, S4P and Fig. 3M). These data suggest that appropriate pGluA1 S831 may promote GluA1 insertion into postsynapses in early stage of AD,

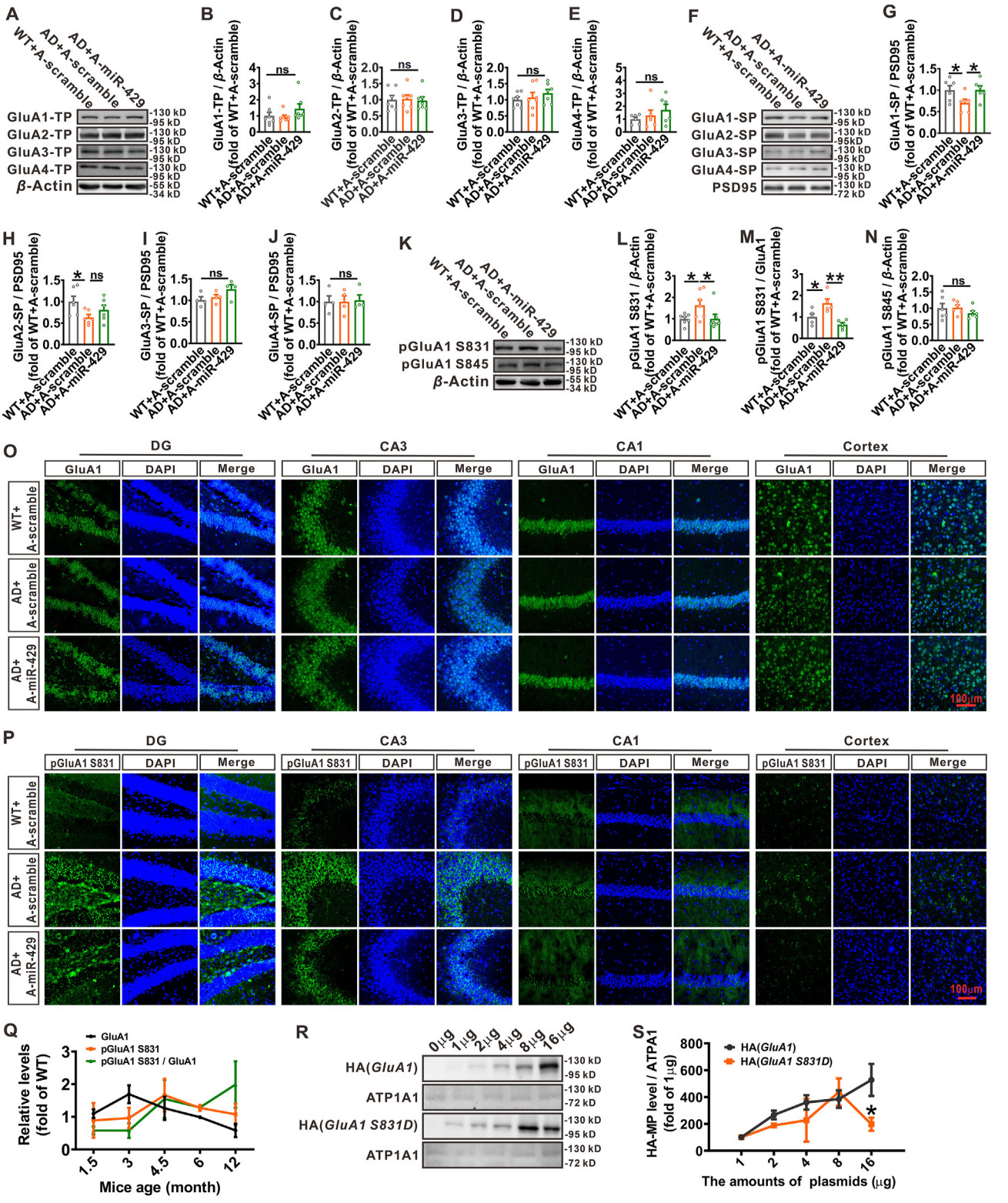

Figure 3 A-miR-429 increases the surface expression of GluA1 in APP23/PS45 mice. (A)−(J) Protein levels of total GluA1 (B), GluA2 (C), GluA3 (D), GluA4 (E), synaptic GluA1 (G) and synaptic GluA2 (H), synaptic GluA3 (I), synaptic GluA4 (J) in APP23/PS45 mice treated with A-miR-429 or A-scramble ($n = 4-7$). (K)−(N) Protein levels of total pGluA1 S831 (L), the ratio of pGluA1 S831 and total GluA1 (M) and total pGluA1 S845 (N) in APP23/PS45 mice treated with A-miR-429 or A-scramble ($n = 5-7$). (O)−(P) Immunofluorescent staining for GluA1 and pGluA1 S831 in APP23/PS45 mice treated with A-miR-429 or A-scramble. Scale bar, 100 μm. (Q) The relative levels of total GluA1, pGluA1 S831 and the ratio of pGluA1 S831 and total GluA1 in APP23/PS45 mice of different ages. (R)−(S) Protein levels of surface HA-tagged GluA1 in N2A cells transfected with 1−16 μg of *GluA1-HA* or *GluA1-S831D-HA* plasmid ($n = 7$). Data are expressed as mean ± SEM. ns, not significant; $^*P < 0.05$, $^{**}P < 0.01$.

whereas excessive pGluA1 S831 may lead to GluA1-containing AMPARs redistribution and reduce surface GluA1 in late stage of AD. To further verify this hypothesis, we constructed a *pGluA1 S831* mimic plasmid with the 831 site mutated from serine to aspartic acid (*GluA1 S831D*). Then, 1−16 μg of HA-tagged *GluA1 or GluA1 S831D* plasmid was individually transfected into the N2A cells and the membrane GluA1 was detected. The results showed that GluA1 in the membrane was increased in a dose-dependent manner with increasing amount of *GluA1* plasmid transfected (Fig. 3R and S), whereas it showed an inverted-U curve and peaked at 8 μg after transfection of *GluA1 S831D* plasmid. Collectively, these results indicate that hyperphosphorylation at the S831 site of GluA1 may inhibit the surface expression and trafficking of GluA1-containing AMPARs.

3.4. Inhibition of miR-429-3p reduces ERK1/2-mediated hyperphosphorylation of GluA1 S831

Next, we wanted to determine what causes *miR-429-3p*-mediated downregulation of MKP-1 to reduce the protein expression of surface GluA1 in AD. In our recent study, we have reported that ERK1/2 is abnormally hyperactivated in AD and overexpression of MKP-1 could rescue the synaptic function by dephosphorylation and inactivation of ERK1/2[15]. Thus, it is reasonable to speculate that the hyperphosphorylation of GluA1 S831 may be related to the hyperactivation of ERK1/2. We next detected the protein expression of pERK1/2, and found that the level of pERK1/2 was significantly higher in AD model mice than that in WT mice (AD + A-scramble: $n = 3$, 1.53 ± 0.06, $P = 0.024$ *vs.* WT + A-scramble; Fig. 4A), A-miR-429 could rescue the level of pERK1/2 to the normal level (AD + A-miR-429: $n = 3$, 1.07 ± 0.11, $P = 0.040$ *vs.* AD + A-scramble, $P = 0.713$ *vs.* WT + A-scramble; Fig. 4A). The protein levels of total ERK1/2 were no significance among three groups ($n = 3$; Fig. 4B). Similar to the finding in the brain of AD model mice, the level of pGluA1 S831 was higher in $N2A^{APP}$ cells than that in N2A cells ($N2A^{APP}$: $n = 3-4$, 2.19 ± 0.11, $P = 0.002$ *vs.* N2A; Fig. 4C). To determine whether ERK1/2 was involved in hyperphosphorylation of GluA1 S831, we treated $N2A^{APP}$ cells with U0126 (ab120241, Abcam, 10 μmol/L), an ERK1/2 inhibitor. The results showed that U0126 treatment significantly reduced the level of pGluA1 S831 (U0126: $n = 4$, 0.26 ± 0.08, $P = 0.016$ *vs.* Ctrl; Fig. 4D) and increased the surface expression of GluA1 (U0126: $n = 6$, 1.54 ± 0.14, $P = 0.028$ *vs.* Ctrl, Fig. 4E). Given that MKP-1 could inactivate ERK1/2 [15], we next investigated the effect of MKP-1 on GluA1 S831 phosphorylation and surface expression level. The results showed that overexpression of MKP-1 reduced the levels of pERK1/2 (MKP-1: $n = 4$, 0.56 ± 0.14, $P = 0.044$ *vs.* Ctrl; Fig. 4F) and pGluA1 S831 (MKP-1: $n = 3$, 0.71 ± 0.09, $P = 0.047$ *vs.* Ctrl; Fig. 4H), as well as upregulated the surface GluA1 subunit of AMPAR (MKP-1: $n = 4$, 1.69 ± 0.22, $P = 0.043$ *vs.* Ctrl; Fig. 4I), but did not alter the protein level of total ERK1/2 in $N2A^{APP}$ cells ($n = 5$; Fig. 4G). Similar to overexpression of MKP-1, A-miR-429 treatment significantly reduced pERK1/2 (A-miR-429: $n = 7$, 0.70 ± 0.06, $P = 0.045$ *vs.* A-scramble; Fig. 4J) and pGluA1 S831 level (A-miR-429: $n = 4$, 0.49 ± 0.10, $P = 0.048$ *vs.* A-scramble; Fig. 4L), and increased the surface level of GluA1 (A-miR-429: $n = 5$, 2.27 ± 0.44, $P = 0.036$ *vs.* A-scramble; Fig. 4M) compared with its scramble (A-scramble) in $N2A^{APP}$ cells. The protein expression of total ERK1/2 remained unchanged with or without A-miR-429 treatment ($n = 4$; Fig. 4K). Collectively, these results suggest that A-miR-429 could restore the surface level of GluA1-containing AMPARs by inhibiting the hyperphosphorylation of GluA1 S831 through MKP-1−ERK1/2 signaling pathway.

3.5. Inhibition of miR-429-3p reduces Aβ-induced impairment of synaptic transmission in primarily cultured neurons

The aforementioned results have demonstrated that inhibition of *miR-429-3p* by A-miR-429 is able to promote GluA1 synaptic localization in AD model mice. Next, we wanted to determine if A-miR-429 can improve Aβ-induced impairment of synaptic transmission in primarily cultured neurons. The results showed that the protein level of MKP-1 was decreased (Aβ+A-scramble: $n = 6$, 0.69 ± 0.08, $P = 0.047$ *vs.* A-scramble; Fig. 5A and B), whereas blockade of *miR-429-3p* with A-miR-429 rescued the level of MKP-1 (Aβ+A-miR-429: $n = 6$, 1.01 ± 0.05, $P = 0.039$ *vs.* Aβ+A-scramble, $P = 0.930$ *vs.* A-scramble; Fig. 5A and B) in the primarily cultured neurons treated with Aβ for 24 h. Consistent with results *in vivo*, no difference in the protein levels of total GluA1 and GluA2 was observed among these three groups (Fig. 5A, C and D). However, membrane expression of GluA1 (Aβ+A-scramble: $n = 6$, 0.58 ± 0.05, $P = 0.006$ *vs.* A-scramble; Fig. 5E and F), but not GluA2 (Fig. 5E and G), was significantly decreased in primarily cultured neurons subjected to Aβ treatment. Importantly, A-miR-429 treatment inhibited Aβ-induced decrease in membrane expression of GluA1 (Aβ+A-miR-429: 0.90 ± 0.08, $P = 0.027$ *vs.* Aβ+A-scramble, $P = 0.463$ *vs.* A-scramble; Fig. 5E and F). Considering the critical function of AMPAR in mediating basal synaptic transmission[36], we next recorded the mEPSCs using whole-cell voltage-clamp recordings in the primarily cultured neurons. The results showed that Aβ treatment significantly decreased mEPSC amplitude (A-scramble: $n = 7$, 23.19 ± 2.35 pA; Aβ+A-scramble: $n = 9$, 16.84 ± 1.01 pA, $P = 0.028$ *vs.* A-scramble; Fig. 5H and I), but did not alter mEPSC frequency (Fig. 5H and J). The decreased mEPSCs amplitude induced by Aβ was able to be fully restored by A-miR-429 treatment (Aβ+A-miR-429: $n = 9$, 22.11 ± 2.12 pA, $P = 0.049$ *vs.* Aβ+A-scramble, $P = 0.692$ *vs.* A-scramble; Fig. 5H and I).

3.6. Inhibition of miR-429-3p reduces the impairments of hippocampal LTP and spatial learning and memory in AD model mice

Since above results suggest that inhibition of *miR-429-3p* by A-miR-429 is able to increase MKP-1-mediated surface GluA1 and basal synaptic transmission *in vitro*, we next wanted to determine whether A-miR-429 can improve synaptic plasticity and cognitive functions in AD model mice. Two-month-old APP23/PS45 double transgenetic AD model mice were intranasally administered with A-miR-429 (1 nmol per mouse) or A-scramble every two days. Two months later, hippocampal CA1 LTP and spatial learning and memory were examined. The results showed that LTP in the hippocampal CA1 region was significantly decreased in AD model mice compared with the WT mice (WT + A-scramble: $n = 5$ slices from 5 mice, $154.21 \pm 10.21\%$ baseline; AD + A-scramble: $n = 8$ slices from 4 mice, $109.35 \pm 4.64\%$ baseline, $P = 0.001$ *vs.* WT + A-scramble; Fig. 6A and B). Importantly, inhibition of *miR-429-3p* by A-miR-429 restored the impaired LTP to WT level in AD model mice (AD ± A-miR-429: $n = 5$ slices from 4 mice, $134.65 \pm 8.79\%$ baseline, $P = 0.026$ *vs.* AD + A-scramble, $P = 0.106$ *vs.* WT + A-scramble; Fig. 6A and B).

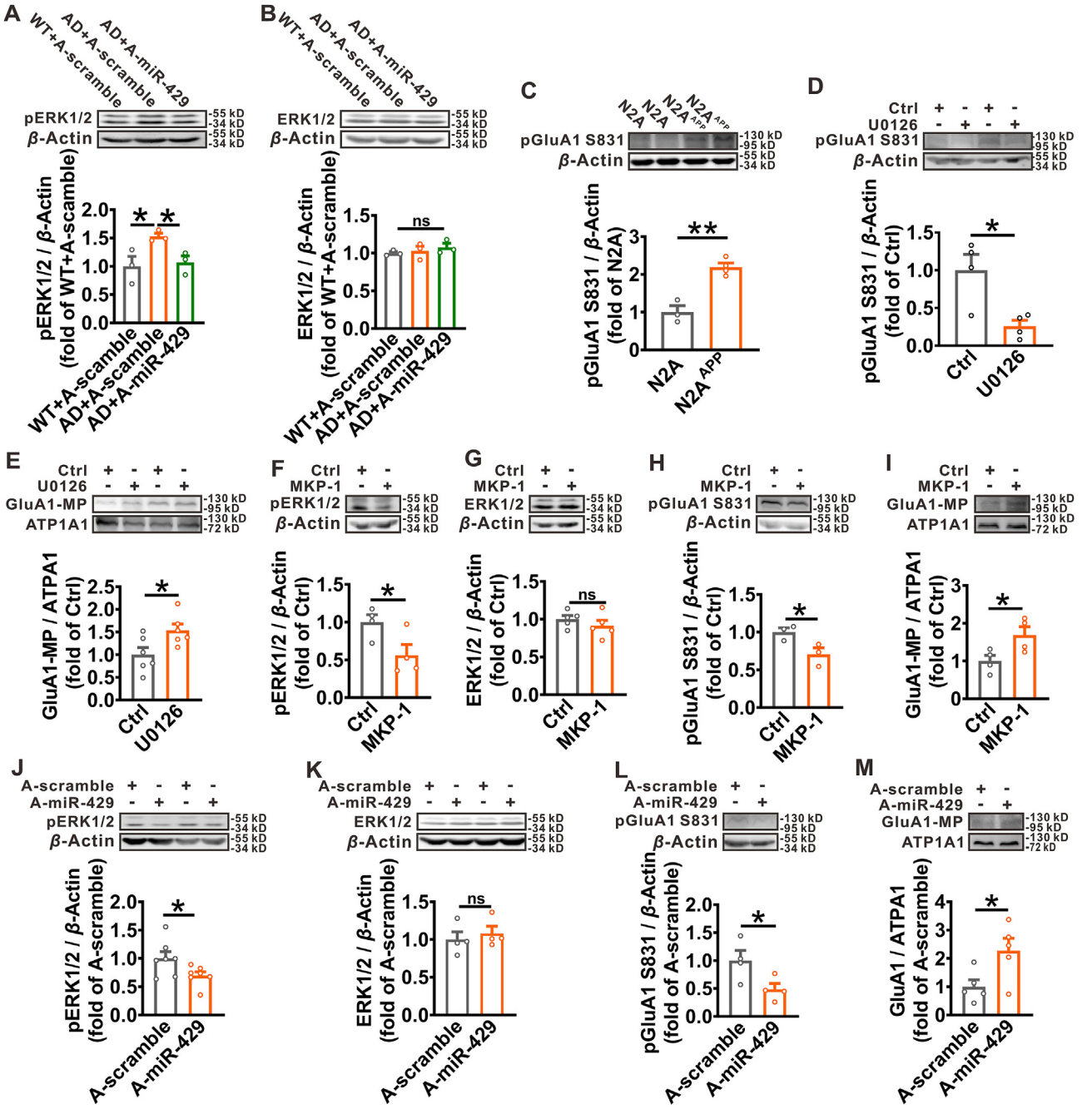

Figure 4 A-miR-429 increases the surface expression of GluA1 by inhibiting MKP-1−ERK1/2-mediated hyperphosphorylation of GluA1 S831. (A, B) Protein levels of pERK1/2 (A) and ERK1/2 (B) in APP23/PS45 mice treated with A-miR-429 or A-scramble (n = 3). (C) The protein expression of total pGluA1 S831 in N2A and $N2A^{APP}$ cells (n = 3−4). (D, E) Protein levels of pGluA1 S831 (D) and surface GluA1 (E) in $N2A^{APP}$ cells treated with U0126 (n = 4−6). (F)−(I) Protein levels of pERK1/2 (F), total ERK1/2 (G), pGluA1 S831 (H) and surface GluA1 (I) in $N2A^{APP}$ cells transfected with *Mkp-1* plasmid or its control (n = 3−5). (J)−(M) Protein levels of pERK1/2 (J), total ERK1/2 (K), pGluA1 S831 (L) and the surface GluA1 (M) in $N2A^{APP}$ cells transfected with A-miR-429 or its A-scramble (n = 3−6). Data are expressed as mean ± SEM. ns, not significant; $^*P < 0.05$, $^{**}P < 0.01$.

To directly examine whether A-miR-429 could alleviate cognitive impairments in AD model mice, the Barnes maze and Morris water maze tests were introduced to measure the spatial learning and memory. In Barnes maze test, the spatial learning was markedly impaired in AD model mice (AD + A-scramble: n = 12, P = 0.001 *vs.* WT + A-scramble; Fig. 6C and D), compared with WT mice (WT + A-scramble: n = 16), as reflected by a longer time to find the escape box during spatial learning period. As expected, A-miR-429 treatment significantly shortened the escape latency to the escape box, especially on Days 4 and 5 (Day 4: AD + A-miR-429: 101.15 ± 15.92, AD + A-scramble:143.29 ± 14.29, P = 0.049 *vs.* AD + A-scramble, P = 0.056 *vs.* WT + A-scramble; Day 5: AD + A-miR-429: 72.94 ± 16.40, AD + A-scramble:139.25 ± 11.21, P = 0.001 *vs.*

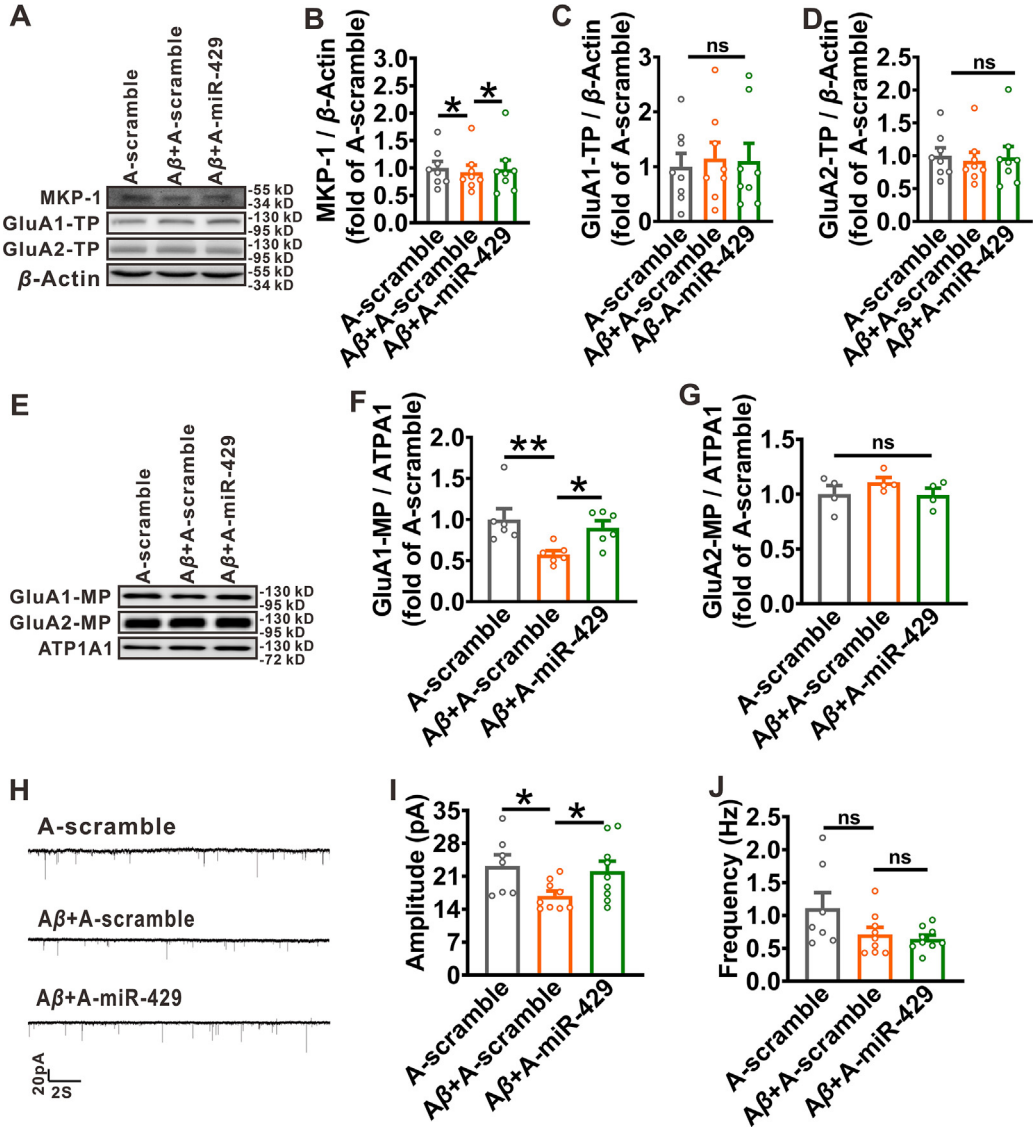

Figure 5 A-miR-429 improves synaptic transmission by increasing the surface expression of GluA1 in primary neurons. (A)−(D) Protein levels of MKP-1 (B), total GluA1 (C) and total GluA2 (D) in primarily cultured neurons transfected with A-miR-429 or A-scramble and treated with 10 μmol/L Aβ (n = 6−8). (E)−(G) Protein levels of surface GluA1 (F) and surface GluA2 (G) in primarily cultured neurons transfected with A-miR-429 or A-scramble and treated with Aβ (10 μmol/L) (n = 4−6). (H)−(J) The amplitude (I) and frequency (J) of mEPSCs are measured by whole-cell recording in cultured neurons transfected with A-miR-429 or A-scramble and treated with Aβ (10 μmol/L) (n = 7−9). Data are expressed as mean ± SEM; *P < 0.05, **P < 0.01, ns, not significant.

AD + A-scramble, P = 0.063 *vs.* WT + A-scramble; Fig. 6C and D). Twenty-four hours after the last training, a long-term spatial memory retrieval test with the escape box blocked was performed. Compared to WT mice, AD mice showed decreased accuracy in finding escape box (WT + A-scramble: 16.17 ± 2.53%; AD + A-scramble: 4.43 ± 1.70%, P = 0.007 *vs.* WT + A-scramble; Fig. 6E), whereas A-miR-429 treatment restored the accuracy to WT level (AD + A-miR-429: 16.06 ± 3.86%, P = 0.985 *vs.* WT + A-scramble, P = 0.022 *vs.* AD + A-scramble; Fig. 6E).

To further evaluate the effect of A-miR-429 on amelioration of memory deficits in AD model mice, we performed another hippocampus-dependent learning and memory task, the Morris water maze test. During the Morris water maze training, the escape latency in AD model mice (AD + A-scramble: n = 11, P < 0.001 *vs.* WT + A-scramble; Fig. 6F and G) was much longer than those in WT mice (WT + A-scramble: n = 13). Consistent with the results in Barnes test, A-miR-429 treatment significantly lessened the escape latency in AD model mice (AD + A-miR-429: n = 11, P = 0.051 *vs.* WT + A-scramble, p = 0.048 *vs.* AD + A-scramble; Fig. 6F and G). Twenty-four hours after the last training trial, a probe test with the platform removed was performed to test memory retention. The number of entries into the platform zone was significantly reduced in the AD model mice compared to WT (WT + A-scramble: 3.85 ± 0.37; AD + A-scramble: 1.64 ± 0.39, P < 0.001 *vs.* WT + A-scramble; Fig. 6H), whereas A-miR-429 treatment increased the entries into the platform zone in AD model mice (AD + A-miR-429: 2.82 ± 0.38, P = 0.062 *vs.* WT + A-scramble, P = 0.040 *vs.* AD + A-scramble; Fig. 6H). To further determine the effects of A-miR-429 on other behaviors besides spatial learning and memory, the open field test, tail-flick

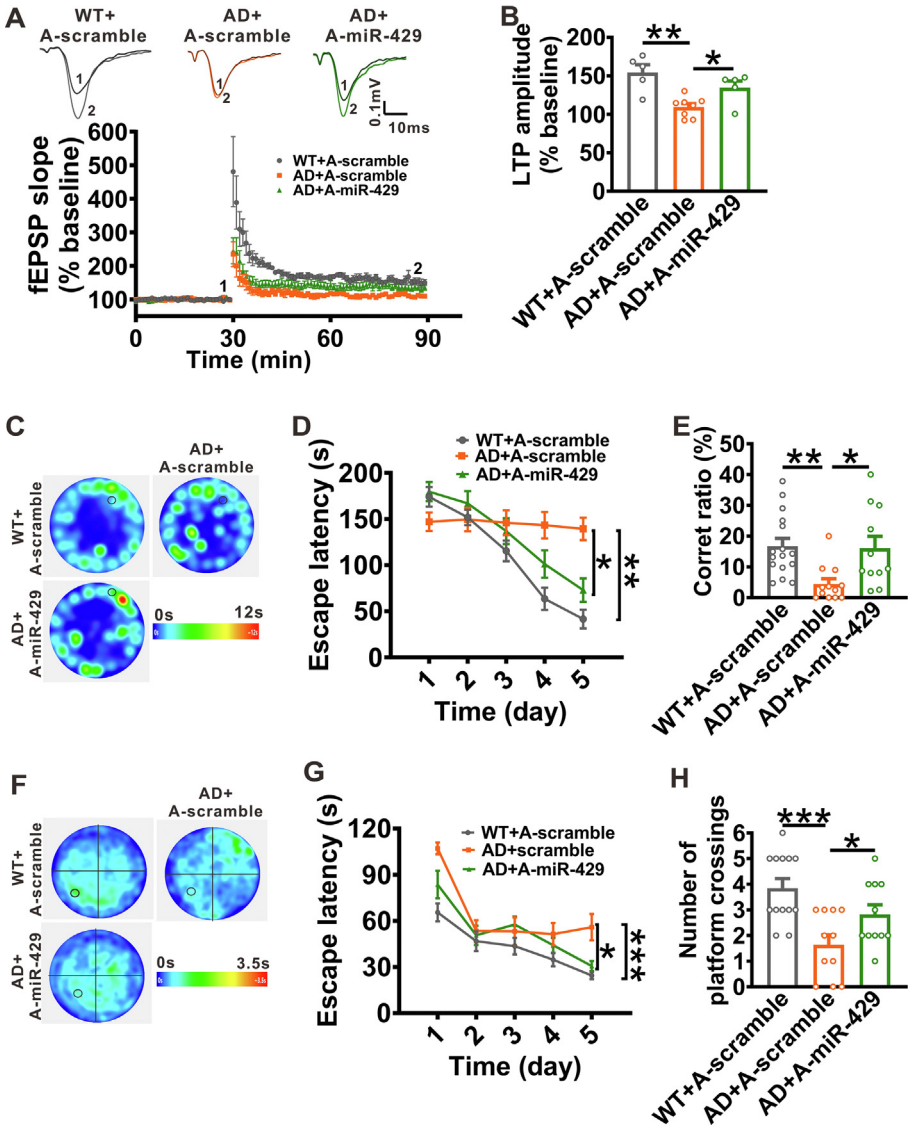

Figure 6 A-miR-429 alleviates the impairments of hippocampus LTP and spatial learning and memory in APP23/PS45 mice. (A) Representative fEPSP traces and plots of the normalized slopes of the fEPSP 5 min before and 55 min after TBS delivery. (B) The bar graphs of the average percentage changes in the fEPSP slope 55−60 min after TBS delivery (n = 5−8 slices from 4 to 5 mice). (C) Average heatmap during memory retrieval in the Barnes maze test. (D) The latency to the escape box during spatial learning in the Barnes maze paradigm (n = 11−16). (E) The accuracy of finding the escape box during memory retrieval. (F) Average heatmap during memory retrieval in the Morris maze test. (G) The escape latency for finding the hidden platform during spatial learning in the Morris maze paradigm (n = 11−13). (H) The number of entries into the platform zone during memory retrieval. Data are expressed as mean ± SEM; *$P < 0.05$, **$P < 0.01$, ***$P < 0.001$, ns, not significant.

test and elevated-plus maze test were introduced to measure the locomotor activity and anxiety/depressive-like behaviors. Notably, the results showed that both locomotor activity and anxiety/depressive-like behaviors remained unchanged in AD model mice treated with A-miR-429 or its control compared to WT mice (Supporting Information Fig. S5).

Taken together, these results demonstrate that inhibition of *miR-429-3p* by A-miR-429 ameliorates the hippocampal CA1 LTP impairment and memory decline in AD model mice.

4. Discussion

Our recent report has found that MKP-1 is markedly down-regulated, and genetic overexpression of MKP-1 is able to inhibit the expression of both APP and BACE1 by inactivating the extracellular signal-regulated kinase 1/2 (ERK1/2)/MAPK signaling pathway, thereby reducing Aβ production in AD model mice[15]. However, the upstream signals leading to the down-regulation of MKP-1 expression in AD are not very clear. In recent years, a growing body of evidence has demonstrated that miRNAs, a class of small non-coding RNAs ~22 nucleotides in length, perform their biological functions by inactivating specific gene expression through either degradation of the target mRNA or direct inhibition of translation[37,38]. Approximately 70% of known miRNAs are expressed in the human nervous system and are closely related to neuronal development, learning and memory, synaptic plasticity, neuroinflammation and so on[39,40]. Recent research progress has shown that several miRNAs are aberrantly expressed in patients with AD or AD mouse models[41−43]. Therefore, it is reasonable to speculate that inhibition of miRNAs that directly bind

to the MKP-1 may benefit AD. Several previous studies have revealed that *miR-101* regulates the innate immune responses of macrophages to LPS[19] and exerts proinflammatory effect[44] through targeting MKP-1, whereas we did not observe any difference in the expression of *miR-101* in the brain between APP23/PS45 double transgenic mice and their littermate controls in the present study. It has been reported that *miR-429* is overexpressed in the hippocampus of 3xTg AD mouse model of AD[45] and in the cerebral cortex of APP/PS1 mouse model of AD[46], while knockdown of *miR-429* attenuates Aβ-induced cytotoxicity by targeting SOX2 and BCL2 in mouse cortical neurons[46]. Nonetheless, contradictory reports challenge these findings. Liu and colleagues[47] reported that *miR-429* is downregulated in the hippocampus of APP/PS1 transgenic mice compared with the WT controls and possibly targets the 3′UTR of *App*. Given this controversy, it is essential to determine the expression of *miR-429* in different AD mouse models and cells and its further potential mechanisms in AD. In this study, we found that *miR-429-3p* was significantly upregulated in the hippocampus of APP23/PS45 mouse model of AD and $N2A^{APP}$ cells, and directly targeted the 3′ UTR of *Mkp-1* and repressed its expression (Fig. 1). Inhibition of *miR-429-3p* by its antagomir (A-miR-429) succeeded in restoring MKP-1 expression to control level, thereby reducing Aβ generation by suppressing the expression of APP and its secretases including BACE1 and PS1 (Fig. 2), suggesting that *miR-429-3p* inhibition may play a neuroprotective role by directly targeting MKP-1 in AD. Notably, we also found that in addition to *miR-429-3p*, the expression of the *miR-200* families such as *miR-200b-3p* and *miR-200c-3p* was markedly upregulated in the mouse model of AD, which was also contradictory in the previous reports[47]. Although it binds directly to *Mkp-1*, *miR-200b/c* mimics or antagomirs could not affect the expression of MKP-1 (Fig. S2). Therefore, its underlying mechanisms need to be addressed in future studies.

AD is an age-related neurodegenerative disease characterized by progressive memory decline and cognitive dysfunction. Synaptic plasticity, an activity-dependent adjustment in the efficacy and strength of synaptic transmission between neurons, is widely thought to contribute to learning and memory. It has been well documented that Aβ could disrupt excitatory synaptic transmission that is mainly medicated by AMPARs, leading to impairment of synaptic plasticity such as LTP[9,48]. It is generally agreed that recruitment and retention of GluA1 and GluA2 AMPARs at synapses are critical for the induction and maintenance of LTP[25,49,50]. Given that A-miR-429 is able to reduce Aβ generation by inhibiting the amyloidogenic processing of APP (Fig. 2), it is reasonable to speculate that A-miR-429 may improve hippocampal LTP through maintaining GluA1-GluA2 AMPARs at the postsynapses. Indeed, we here found that synaptic amounts of both GluA1 and GluA2 were significantly decreased in the hippocampus of AD model mice compared to WT mice, while A-miR-429 administration restored the expression of GluA1, but not GluA2, to control level at the postsynapses (Fig. 3). In addition to the amount of AMPARs, phosphorylation of two sites on the GluA1 subunit, serine 831 (GluA1 S831) and serine 845 (GluA1 S845), recruits AMPARs to the synapse to potentiate AMPAR ion channel function[51,52]. Mutations that disable both phosphorylation sites increase AMPAR internalization[53], and consequently impair hippocampal CA1 LTP together with long-term retention of spatial memory task[30] as well as appetitive incentive learning[54] in mice. Consistent with a previous report[55], we found a marked reduction in phosphorylation of GluA1 in the early stage of AD in the present study (Fig. 3). Meanwhile, in line with our results (Fig. 3), several lines of evidence also indicate that GluA1 phosphorylation on Ser831 (pGluA1 S831), but not GluA1 Ser845 (pGluA1 S845), is essential for LTP production[56]. Although it is well studied that the phosphorylation of GluA1 S831 is mediated by Ca^{2+}/calmodulin-dependent protein kinase II (CaMKII) or protein kinase C (PKC)[57,58], Ras-ERK1/2 signaling is also thought to be crucial for AMPAR recruitment to spines following LTP induction, as inhibition of Ras or ERK1/2 blocks phosphorylation of GluA1 and LTP production[59]. However, ERK1/2 is hyperactivated in the late stage of AD, and inhibition of ERK1/2 overactivation by MKP-1 can reverse memory decline in AD model mice[15]. It is therefore reasonable to speculate that in the late stage of AD, hyperactivated ERK1/2 leads to an excessive increase in pGluA1 S831, which subsequently may induce impairment of GluA1 trafficking and synaptic localization. Indeed, we here report that the pGluA1 S831 was dramatically increased in the brain of AD model mice, which can be restored by A-miR-429 treatment (Fig. 3). We have found U0126, an ERK1/2 inhibitor, could significantly decrease the level of phosphorylation of GluA1 S831 and promote the surface expression of GluA1. More importantly, A-miR-429, as the regulator of MKP-1, could devitalize ERK1/2 and reduce the phosphorylation level of GluA1 S831, thereby increasing surface GluA1-containing AMPARs in $N2A^{APP}$ cells (Fig. 4). In addition to directly phosphorylating GluA1 at the S831 site, ERK1/2 may also activate other kinases, such as PKC by inducing translocation of PKC to the plasma membrane[60]. Similar to the hypophosphorylation of GluA1 S831 inhibiting its trafficking and redistribution, hyperphosphorylation of GluA1 S831 can also disrupt its normal trafficking process. For example, nitrosylation of GluA1 at cysteine 875 induces the phosphorylation of GluA1 on S831 site, leading to endocytosis of the GluA1-containing AMPARs by increasing receptor binding to the AP2 protein of the endocytotic machinery[61,62]. In addition, hyperphosphorylation of GluA1 S831 does not affect AMPAR-trafficking-vesicle transport speed, but causes more vesicles to pause[63]. Disruption of GluA1 phosphorylation, especially at site of S831[29,64,65], inhibits the increase in GluA1 number and GluA1 exocytosis frequency in both postsynaptic and extrasynaptic membranes[66]. Combined with the latest research advances, our results suggest that *miR-429-3p*−MKP-1−ERK1/2-mediated hyperphosphorylation of GluA1 S831 disrupts its normal trafficking, thereby reducing the surface expression of GluA1 in AD. However, whether GluA1 endocytosis is increased or membrane insertion is decreased during this process, and the underlying molecular mechanisms, need to be further investigated in the future.

5. Conclusions

Our study demonstrates that the *miR-429-3p*/MKP-1 signaling pathway plays a critical role in the pathogenesis of AD (Fig. 7). In the present study, we found that age-dependent Aβ production can inhibit the expression of MKP-1 through *miR-429-3p*, which promotes APP amyloidogenic processing and Aβ aggregation through the ERK1/2 signaling pathway. In turn, increased Aβ may further inhibit MKP-1 by increasing *miR-429-3p*, thereby forming a circle. Although the specific mechanism of this circle formation needs to be further explored, our findings show that inhibition of *miR-429-3p* reduces the amyloidogenic processing of APP and ameliorates synaptic and cognitive functions by upregulating MKP-1 in a mouse model of AD. Thus, our study provides potential therapeutics for treating the learning and memory deficits

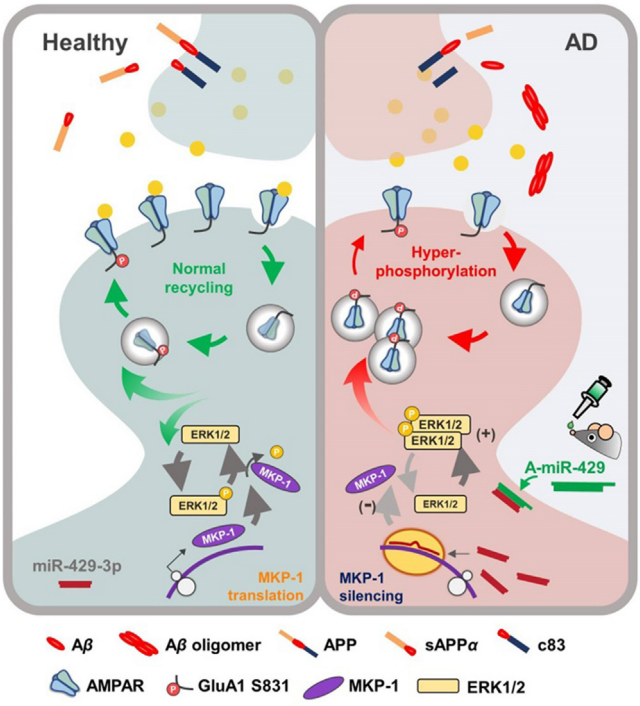

Figure 7 Schematic illustration presumed the mechanism of *miR-429-3p* in AD. *miR-429-3p* is significantly increased in AD and downregulates the expression of MKP-1 through directly binding to its 3′UTR, thereby resulting in overactivation of ERK1/2, which leads to hyperphosphorylation of GluA1 S831. Hyperphosphorylation of GluA1 S831 disrupts normal trafficking and distribution, resulting in a reduction of surface GluA1-containing AMPARs, thereby disrupting synaptic and cognitive functions.

associated with both patients with AD and aged populations by intranasal administration of A-miR-429.

Acknowledgements

This work was supported by grants from the National Natural Science Foundation of China (32371030, 82371194, 82071395 and 82001158), the Natural Science Foundation of Chongqing (CSTB2022NSCQ-LZX0010 and cstc2021ycjh-bgzxm0186, China), the Scientific and Technological Innovation Project for the Construction of Chengdu-Chongqing Economic Circle (KJCX ZD2020021, China) and CQMU Program for Youth Innovation in Future Medicine (W0044, China). We are grateful to other members in the Dong laboratory for the technical support and helpful suggestion.

Author contributions

Zhifang Dong and Yehong Du conceived and designed this project. Man Luo, Lilin Yi, Qiuyun Tian and Bin Wu performed behavioral and biochemical experiments. Yan He and Maoju Wang constructed plasmids. Junjie Li, Yayan Pang and Lei Xia performed electrophysiological studies. Man Luo analyzed the data. Zhifang Dong, Yehong Du and Weihong Song contributed essential reagents or tools. WS provided important discussions and suggestions. Man Luo, Yehong Du, Guiqiong He and Zhifang Dong wrote the manuscript. All authors reviewed and edited the manuscript and approved the final version.

Conflicts of interest

The authors declare no conflicts of interest.

Appendix A. Supporting information

Supporting data to this article can be found online at https://doi.org/10.1016/j.apsb.2023.10.015.

References

1. Colvin MT, Silvers R, Frohm B, Su Y, Linse S, Griffin RG. High resolution structural characterization of $A\beta_{42}$ amyloid fibrils by magic angle spinning NMR. *J Am Chem Soc* 2015;**137**:7509−18.
2. Austad SN, Ballinger S, Buford TW, Carter CS, Smith Jr DL, Darley-Usmar V, et al. Targeting whole body metabolism and mitochondrial bioenergetics in the drug development for Alzheimer's disease. *Acta Pharm Sin B* 2022;**12**:511−31.
3. Kim J, Basak JM, Holtzman DM. The role of apolipoprotein E in Alzheimer's disease. *Neuron* 2009;**63**:287−303.
4. O'Brien RJ, Wong PC. Amyloid precursor protein processing and Alzheimer's disease. *Annu Rev Neurosci* 2011;**34**:185−204.
5. Troncone L, Luciani M, Coggins M, Wilker EH, Ho CY, Codispoti KE, et al. Abeta amyloid pathology affects the hearts of patients with Alzheimer's disease: mind the heart. *J Am Coll Cardiol* 2016;**68**:2395−407.
6. He C, Huang ZS, Yu CC, Wang HH, Zhou H, Kong LH. Epigenetic regulation of amyloid-beta metabolism in Alzheimer's disease. *Curr Med Sci* 2020;**40**:1022−30.
7. Baranger K, Bonnet AE, Girard SD, Paumier JM, Garcia-Gonzalez L, Elmanaa W, et al. MT5-MMP promotes Alzheimer's pathogenesis in the frontal cortex of 5xFAD mice and APP trafficking *in vitro*. *Front Mol Neurosci* 2016;**9**:163.
8. Willem M, Tahirovic S, Busche MA, Ovsepian SV, Chafai M, Kootar S, et al. η-Secretase processing of APP inhibits neuronal activity in the hippocampus. *Nature* 2015;**526**:443−7.
9. Shankar GM, Li S, Mehta TH, Garcia-Munoz A, Shepardson NE, Smith I, et al. Amyloid-beta protein dimers isolated directly from Alzheimer's brains impair synaptic plasticity and memory. *Nat Med* 2008;**14**:837−42.
10. Padmanabhan P, Kneynsberg A, Gotz J. Super-resolution microscopy: a closer look at synaptic dysfunction in Alzheimer disease. *Nat Rev Neurosci* 2021;**22**:723−40.
11. Jeanneteau F, Deinhardt K, Miyoshi G, Bennett AM, Chao MV. The MAP kinase phosphatase MKP-1 regulates BDNF-induced axon branching. *Nat Neurosci* 2010;**13**:1373−9.
12. Boutros T, Chevet E, Metrakos P. Mitogen-activated protein (MAP) kinase/MAP kinase phosphatase regulation: roles in cell growth, death, and cancer. *Pharmacol Rev* 2008;**60**:261−310.
13. Collins LM, Downer EJ, Toulouse A, Nolan YM. Mitogen-activated protein kinase phosphatase (MKP)-1 in nervous system development and disease. *Mol Neurobiol* 2015;**51**:1158−67.
14. Gu Y, Ma LJ, Bai XX, Jie J, Zhang XF, Chen D, et al. Mitogen-activated protein kinase phosphatase 1 protects PC12 cells from amyloid beta-induced neurotoxicity. *Neural Regen Res* 2018;**13**:1842−50.
15. Du Y, Du Y, Zhang Y, Huang Z, Fu M, Li J, et al. MKP-1 reduces $A\beta$ generation and alleviates cognitive impairments in Alzheimer's disease models. *Signal Transduct Targeted Ther* 2019;**4**:58.
16. Dehghani R, Rahmani F, Rezaei N. MicroRNA in Alzheimer's disease revisited: implications for major neuropathological mechanisms. *Rev Neurosci* 2018;**29**:161−82.
17. Putteeraj M, Fairuz YM, Teoh SL. microRNA dysregulation in Alzheimer's disease. *CNS Neurol Disord: Drug Targets* 2017;**16**:1000−9.
18. Kim B, Tag SH, Nam E, Ham S, Ahn S, Kim J, et al. SYNCRIP controls miR-137 and striatal learning in animal models of methamphetamine abstinence. *Acta Pharm Sin B* 2022;**12**:3281−97.

19. Zhu QY, Liu Q, Chen JX, Lan K, Ge BX. MicroRNA-101 targets MAPK phosphatase-1 to regulate the activation of MAPKs in macrophages. *J Immunol* 2010;**185**:7435−42.
20. Zhang Q, Abouelfetouh MM, Chen S, Li M, Ding M, Ding Y. MicroRNA Let-7b-5p induces electroacupuncture tolerance by downregulating the *MKP-1* gene in rats subjected to CFA-induced inflammatory nociception. *J Mol Neurosci* 2020;**70**:1198−207.
21. Singh GB, Raut SK, Khanna S, Kumar A, Sharma S, Prasad R, et al. MicroRNA-200c modulates DUSP-1 expression in diabetes-induced cardiac hypertrophy. *Mol Cell Biochem* 2017;**424**:1−11.
22. Cao YX, Wang ZQ, Kang JX, Liu K, Zhao CF, Guo YX, et al. miR-424 protects PC-12 cells from OGD-induced injury by negatively regulating MKP-1. *Eur Rev Med Pharmacol Sci* 2018;**22**:1426−36.
23. Ran FA, Hsu PD, Wright J, Agarwala V, Scott DA, Zhang F. Genome engineering using the CRISPR-Cas9 system. *Nat Protoc* 2013;**8**: 2281−308.
24. Chen L, Xu B, Liu L, Luo Y, Yin J, Zhou H, et al. Hydrogen peroxide inhibits mTOR signaling by activation of AMPKα leading to apoptosis of neuronal cells. *Lab Invest* 2010;**90**:762−73.
25. Dong Z, Han H, Li H, Bai Y, Wang W, Tu M, et al. Long-term potentiation decay and memory loss are mediated by AMPAR endocytosis. *J Clin Invest* 2015;**125**:234−47.
26. Bartel DP. MicroRNAs: genomics, biogenesis, mechanism, and function. *Cell* 2004;**116**:281−97.
27. Malenka RC, Bear MF. LTP and LTD: an embarrassment of riches. *Neuron* 2004;**44**:5−21.
28. Whitlock JR, Heynen AJ, Shuler MG, Bear MF. Learning induces long-term potentiation in the hippocampus. *Science* 2006;**313**: 1093−7.
29. Xue B, Chen EC, He N, Jin DZ, Mao LM, Wang JQ. Integrated regulation of AMPA glutamate receptor phosphorylation in the striatum by dopamine and acetylcholine. *Neuropharmacology* 2017;**112**: 57−65.
30. Lee HK, Takamiya K, Han JS, Man H, Kim CH, Rumbaugh G, et al. Phosphorylation of the AMPA receptor GluR1 subunit is required for synaptic plasticity and retention of spatial memory. *Cell* 2003;**112**: 631−43.
31. Diering GH, Heo S, Hussain NK, Liu B, Huganir RL. Extensive phosphorylation of AMPA receptors in neurons. *Proc Natl Acad Sci U S A* 2016;**113**:E4920−7.
32. Lee HK, Kirkwood A. AMPA receptor regulation during synaptic plasticity in hippocampus and neocortex. *Semin Cell Dev Biol* 2011; **22**:514−20.
33. Robert BJA, Moreau MM, Dos Santos Carvalho S, Barthet G, Racca C, Bhouri M, et al. Vangl2 in the dentate network modulates pattern separation and pattern completion. *Cell Rep* 2020; **31**:107743.
34. Battistoni S, Erokhin V, Iannotta S. Emulation with organic memristive devices of impairment of LTP mechanism in neurodegenerative disease pathology. *Neural Plast* 2017;**2017**:6090312.
35. Vitolo OV, Sant'Angelo A, Costanzo V, Battaglia F, Arancio O, Shelanski M. Amyloid beta-peptide inhibition of the PKA/CREB pathway and long-term potentiation: reversibility by drugs that enhance cAMP signaling. *Proc Natl Acad Sci U S A* 2002;**99**:13217−21.
36. Lu HW, Balmer TS, Romero GE, Trussell LO. Slow AMPAR synaptic transmission is determined by stargazin and glutamate transporters. *Neuron* 2017;**96**:73−80 e4.
37. Bartel DP. MicroRNAs: target recognition and regulatory functions. *Cell* 2009;**136**:215−33.
38. Mohr AM, Mott JL. Overview of microRNA biology. *Semin Liver Dis* 2015;**35**:3−11.
39. Nowak JS, Choudhury NR, de Lima Alves F, Rappsilber J, Michlewski G. Lin28a regulates neuronal differentiation and controls miR-9 production. *Nat Commun* 2014;**5**:3687.
40. Cao X, Yeo G, Muotri AR, Kuwabara T, Gage FH. Noncoding RNAs in the mammalian central nervous system. *Annu Rev Neurosci* 2006; **29**:77−103.
41. Liu S, Fan M, Zheng Q, Hao S, Yang L, Qi C, et al. MicroRNAs in Alzheimer's disease: potential diagnostic markers and therapeutic targets. *Biomed Pharmacother* 2022:112681.
42. Tan L, Yu JT, Hu N, Tan L. Non-coding RNAs in Alzheimer's disease. *Mol Neurobiol* 2013;**47**:382−93.
43. Idda ML, Munk R, Abdelmohsen K, Gorospe M. Noncoding RNAs in Alzheimer's disease. *Wiley Interdiscip Rev RNA* 2018;**9**:10.
44. Gao Y, Liu F, Fang L, Cai R, Zong C, Qi Y. Genkwanin inhibits proinflammatory mediators mainly through the regulation of miR-101/MKP-1/MAPK pathway in LPS-activated macrophages. *PLoS One* 2014;**9**:e96741.
45. Barak B, Shvarts-Serebro I, Modai S, Gilam A, Okun E, Michaelson DM, et al. Opposing actions of environmental enrichment and Alzheimer's disease on the expression of hippocampal microRNAs in mouse models. *Transl Psychiatry* 2013;**3**: e304.
46. Fu S, Zhang J, Zhang S. Knockdown of miR-429 attenuates Aβ-induced neuronal damage by targeting SOX2 and BCL2 in mouse cortical neurons. *Neurochem Res* 2018;**43**:2240−51.
47. Liu CG, Wang JL, Li L, Xue LX, Zhang YQ, Wang PC. MicroRNA-135a and -200b, potential biomarkers for Alzheimers disease, regulate β secretase and amyloid precursor protein. *Brain Res* 2014;**1583**: 55−64.
48. Nalbantoglu J, Tirado-Santiago G, Lahsaini A, Poirier J, Goncalves O, Verge G, et al. Impaired learning and LTP in mice expressing the carboxy terminus of the Alzheimer amyloid precursor protein. *Nature* 1997;**387**:500−5.
49. Hayashi Y, Shi SH, Esteban JA, Piccini A, Poncer JC, Malinow R. Driving AMPA receptors into synapses by LTP and CaMKII: requirement for GluR1 and PDZ domain interaction. *Science* 2000; **287**:2262−7.
50. Zamanillo D, Sprengel R, Hvalby O, Jensen V, Burnashev N, Rozov A, et al. Importance of AMPA receptors for hippocampal synaptic plasticity but not for spatial learning. *Science* 1999;**284**: 1805−11.
51. Derkach V, Barria A, Soderling TR. Ca^{2+}/calmodulin-kinase II enhances channel conductance of alpha-amino-3-hydroxy-5-methyl-4-isoxazolepropionate type glutamate receptors. *Proc Natl Acad Sci U S A* 1999;**96**:3269−74.
52. Lee HK, Barbarosie M, Kameyama K, Bear MF, Huganir RL. Regulation of distinct AMPA receptor phosphorylation sites during bidirectional synaptic plasticity. *Nature* 2000;**405**:955−9.
53. Matt L, Pham T, Skrabak D, Hoffmann F, Eckert P, Yin J, et al. The Na^+-activated K^+ channel Slack contributes to synaptic development and plasticity. *Cell Mol Life Sci* 2021;**78**:7569−87.
54. Crombag HS, Sutton JM, Takamiya K, Lee HK, Holland PC, Gallagher M, et al. A necessary role for GluR1 serine 831 phosphorylation in appetitive incentive learning. *Behav Brain Res* 2008; **191**:178−83.
55. Cantanelli P, Sperduti S, Ciavardelli D, Stuppia L, Gatta V, Sensi SL. Age-dependent modifications of AMPA receptor subunit expression levels and related cognitive effects in 3xTg-AD mice. *Front Aging Neurosci* 2014;**6**:200.
56. Rodrigues NC, Silva-Cruz A, Caulino-Rocha A, Bento-Oliveira A, Alexandre Ribeiro J, Cunha-Reis D. Hippocampal CA1 theta burst-induced LTP from weaning to adulthood: cellular and molecular mechanisms in young male rats revisited. *Eur J Neurosci* 2021;**54**: 5272−92.
57. Barria A, Muller D, Derkach V, Griffith LC, Soderling TR. Regulatory phosphorylation of AMPA-type glutamate receptors by CaM-KII during long-term potentiation. *Science* 1997;**276**:2042−5.
58. Malinow R, Schulman H, Tsien RW. Inhibition of postsynaptic PKC or CaMKII blocks induction but not expression of LTP. *Science* 1989; **245**:862−6.
59. Zhu JJ, Qin Y, Zhao M, Van Aelst L, Malinow R. Ras and Rap control AMPA receptor trafficking during synaptic plasticity. *Cell* 2002;**110**: 443−55.

60. Shobe JL, Zhao Y, Stough S, Ye X, Hsuan V, Martin KC, et al. Temporal phases of activity-dependent plasticity and memory are mediated by compartmentalized routing of MAPK signaling in aplysia sensory neurons. *Neuron* 2009;**61**:113−25.
61. Bingor A, Haham T, Thornton C, Stern-Bach Y, Yaka R. Zeta Inhibitory peptide attenuates learning and memory by inducing NO-mediated downregulation of AMPA receptors. *Nat Commun* 2020; **11**:3688.
62. Selvakumar B, Jenkins MA, Hussain NK, Huganir RL, Traynelis SF, Snyder SH. *S*-Nitrosylation of AMPA receptor GluA1 regulates phosphorylation, single-channel conductance, and endocytosis. *Proc Natl Acad Sci U S A* 2013;**110**:1077−82.
63. Hangen E, Cordelieres FP, Petersen JD, Choquet D, Coussen F. Neuronal activity and intracellular calcium levels regulate intracellular transport of newly synthesized AMPAR. *Cell Rep* 2018;**24**:1001−10012 e3.
64. Mao LM, Xue B, Jin DZ, Wang JQ. Dynamic increases in AMPA receptor phosphorylation in the rat hippocampus in response to amphetamine. *J Neurochem* 2015;**133**:795−805.
65. Mao LM, Wang JQ. Upregulation of AMPA receptor GluA1 phosphorylation by blocking adenosine A1 receptors in the male rat forebrain. *Brain Behav* 2020;**10**:e01543.
66. Tanaka H, Sakaguchi D, Hirano T. Amyloid-β oligomers suppress subunit-specific glutamate receptor increase during LTP. *Alzheimers Dement (N Y)* 2019;**5**:797−808.